

---

This is an electronic reprint of the original article.  
This reprint may differ from the original in pagination and typographic detail.

Shen, Fuhui; Münstermann, Sebastian; Lian, Junhe

## An evolving plasticity model considering anisotropy, thermal softening and dynamic strain aging

*Published in:*  
International Journal of Plasticity

*DOI:*  
[10.1016/j.ijplas.2020.102747](https://doi.org/10.1016/j.ijplas.2020.102747)

Published: 01/09/2020

*Document Version*  
Peer-reviewed accepted author manuscript, also known as Final accepted manuscript or Post-print

*Published under the following license:*  
CC BY-NC-ND

*Please cite the original version:*  
Shen, F., Münstermann, S., & Lian, J. (2020). An evolving plasticity model considering anisotropy, thermal softening and dynamic strain aging. *International Journal of Plasticity*, 132, Article 102747.  
<https://doi.org/10.1016/j.ijplas.2020.102747>

---

This material is protected by copyright and other intellectual property rights, and duplication or sale of all or part of any of the repository collections is not permitted, except that material may be duplicated by you for your research use or educational purposes in electronic or print form. You must obtain permission for any other use. Electronic or print copies may not be offered, whether for sale or otherwise to anyone who is not an authorised user.

# **An evolving plasticity model considering anisotropy, thermal softening and dynamic strain aging**

Fuhui Shen<sup>a</sup>, Sebastian Münstermann<sup>a</sup> and Junhe Lian<sup>b,c,\*</sup>

<sup>a</sup>Integrity of Materials and Structures, Steel Institute, RWTH Aachen University,  
Intzestraße 1, 52072 Aachen, Germany

<sup>b</sup>Advanced Manufacturing and Materials, Department of Mechanical Engineering, Aalto  
University, Puumiehenkuja 3, 02150 Espoo, Finland

<sup>c</sup>Impact and Crashworthiness Laboratory, Department of Mechanical Engineering,  
Massachusetts Institute of Technology, 77 Massachusetts Avenue, Cambridge, MA  
02139-4307, USA

\*Phone: +358 50 477 0765

[junhe.lian@aalto.fi](mailto:junhe.lian@aalto.fi); [lianjh@mit.edu](mailto:lianjh@mit.edu)

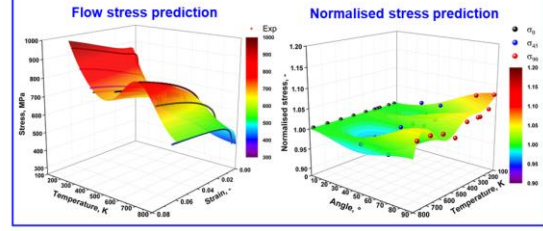
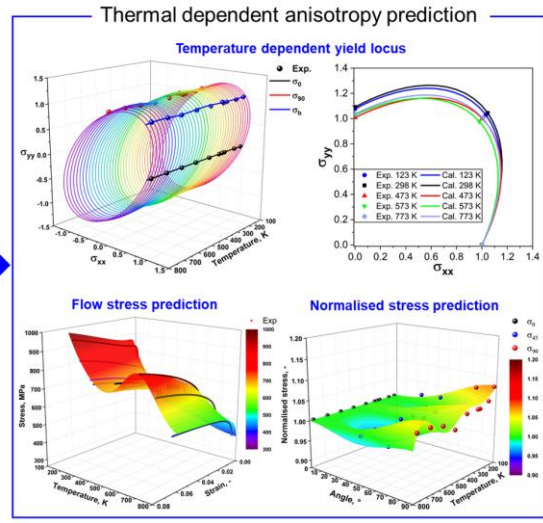
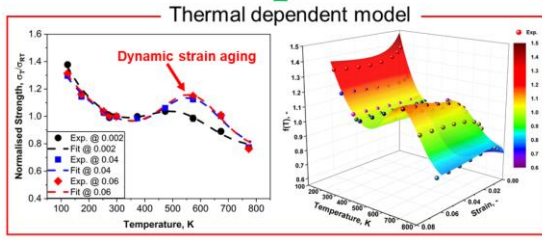
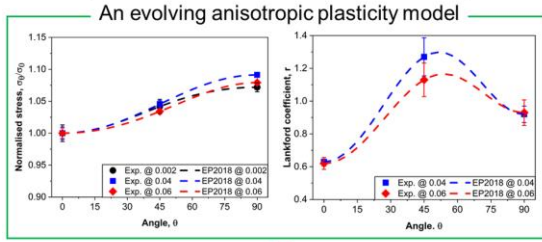
To cite the publications:

Fuhui Shen, Sebastian Münstermann, Junhe Lian, An evolving plasticity model considering anisotropy, thermal softening and dynamic strain aging, International Journal of Plasticity, 2020, 102747, <https://doi.org/10.1016/j.ijplas.2020.102747>.

## **Highlights:**

- Thermal effects on anisotropy of two high-strength steels are characterized from - 150 °C to 500 °C.
- A significant non-monotonic temperature effect on the flow strength is found for both steels due to dynamic strain aging.
- Depending on materials, the stress anisotropy shows a minor or strong dependency on temperature.
- The evolution of anisotropy at different temperatures is strongly affected by the dynamic strain aging effect.
- The evolving non-associated Hill48 model is extended to capture the thermal-dependent anisotropic flow behavior.

# Graphic abstract:



**Abstract:**

Comprehensive experimental characterization and numerical prediction have been performed to investigate the thermal effects on the anisotropic flow behavior of two high-strength steels in this study. For the experimental investigation of the anisotropic plasticity under the influence of temperature, uniaxial tensile tests have been conducted along three different loading directions covering the temperature range from 123 K to 773 K under the quasi-static loading condition. The results show that the thermal effects on the flow behavior are non-monotonic because not only the typical thermal softening but also the dynamic strain aging phenomena are observed. Moreover, the thermal effects on the anisotropy behavior are not constant but strain and material dependent. Regarding the numerical description, a generalized evolving plasticity model considering the evolution of thermal effects on flow behavior is proposed. With all material parameters systematically calibrated following a straightforward approach, the model is used to describe the temperature dependence of anisotropic plastic flow behavior of the investigated materials. The predictive capability of the model is validated by experimental results across a large temperature range even with the activation of complicated deformation mechanisms such as dynamic strain aging.

**Keywords:** Constitutive model; Evolving plasticity; Anisotropy; Thermal softening; Dynamic strain aging

## 1 Introduction

Constitutive models have been playing vital roles in the precise description of the plastic flow behavior of materials. Due to the sufficient accuracy and high simplicity of implementation, various types of phenomenological constitutive models have been developed in the past decades to address distinct aspects of plasticity behavior, such as anisotropy (Banabic et al., 2005; Barlat et al., 2003; Cazacu et al., 2006), loading history (Barlat et al., 2011; Yoshida and Uemori, 2002), flow rule (Safaei et al., 2014; Stoughton, 2002; Stoughton and Yoon, 2009), stress state (Bai and Wierzbicki, 2008; Gao et al., 2011; Park et al., 2019a; Yoon et al., 2014), temperature and strain rate effects (Johnson and Cook, 1985; Khan and Huang, 1992; Khan and Liang, 1999).

The anisotropic plasticity of sheet materials has been a major aspect in the development of plasticity theories. Starting from the first quadratic anisotropic plasticity model proposed by Hill (1948), different types of phenomenological anisotropic constitutive models have been developed. The research group of Barlat has made significant contributions to the modeling of anisotropy by developing a series of yield criteria, such as Yld89 (Barlat and Lian, 1989), Yld91 (Barlat et al., 1991), Yld2000-2d (Barlat et al., 2003), Yld2004-18p (Barlat et al., 2005a) and Yld2011-27p (Aretz and Barlat, 2013). There are also numerous anisotropic models developed and applied widely by other researchers (Banabic et al., 2005; Bron and Besson, 2004; Cazacu, 2018; Gao et al., 2011; Karafillis and Boyce, 1993; Lou and Yoon, 2018; Plunkett et al., 2006). More detailed reviews on the anisotropic constitutive models are available in (Banabic et al., 2010) and (Barlat et al., 2005b). Most of these advanced non-quadratic models are based on the linear transformation method, in which higher accuracy is achieved at the expense of complicated parameter calibration. In conjunction with these yield criteria based on the associated flow rule, the development based on the non-associated flow rule (NAFR) has also gained popularity due to its simple implementation and high flexibility (Lee et al., 2017; Lian et al., 2018b; Park et al.,

2019b; Safaei et al., 2014; Safaei et al., 2013; Stoughton, 2002; Stoughton and Yoon, 2009). In addition to the anisotropic yielding behavior, the evolution of anisotropy due to the microstructural change during plastic deformation (Jeong et al., 2016; Saleh et al., 2013; Xie et al., 2018) has become a sensitive topic to pursue the excellent description of the plastic behavior (Bandyopadhyay et al., 2019; Kondori et al., 2019; Li et al., 2017; Lian et al., 2018a; Lian et al., 2018b; Park et al., 2019b; Suzuki et al., 2018). Considering the evolution of anisotropy with plastic strain, Lian et al. (2018b) demonstrated that improved accuracy is achieved in the forming limit prediction of a ferritic stainless steel using the modified maximum force criterion (MMFC) (Hora et al., 2011), which has been also recently confirmed by Shen et al. (2019b) using the Marciniak–Kuczynski (MK) model (Marciniak and Kuczynski, 1967). Other studies based on the finite element simulation have also verified the significance of evolving features on the anisotropic flow behavior of various materials (Bandyopadhyay et al., 2019; Ha et al., 2018). Most of these models on anisotropy focus on plastic behavior at room temperature. However, the material usually experiences various temperatures in the forming processes or service conditions. The observed macroscopic material responses to temperature variation are governed by complicated mechanisms, such as thermal softening, dynamic recovery, dynamic recrystallization and dynamic strain aging (DSA). The thermal softening is the dominant mechanism for most crystalline materials due to the thermal activation nature of dislocation motion and the temperature dependence of twinning capacity. Liang and Khan (1999), Chaboche (2008) and Sung et al. (2010) have provided reviews on the constitutive models describing the thermal softening effects. The most widely applied phenomenological models include the BP model by Bodner and Partom (1975), the JC model by Johnson and Cook (1985), the ZA model by Zerilli and Armstrong (1987), the KHL model by Khan and Huang (1992) and Khan and Liang (1999), and their modifications. In these models, temperature and strain rate are usually treated

as two independent variables and their influence on flow behavior is included simultaneously. Dependent on the specific formulations as well as the various coupling methods between strain rate and temperature, distinct accuracy is achieved in these models within different ranges of temperature and strain rate. Abedrabbo et al. (2006a, 2006b) have experimentally characterized the influence of temperature on the anisotropy and hardening behavior of aluminum alloys. Khan and his co-workers (Habib et al., 2017; Khan and Baig, 2011; Khan et al., 2007; Khan and Liu, 2012; Khan and Yu, 2012; Khan et al., 2012) have comprehensively investigated the mechanical response of titanium alloys under the influence of anisotropy, stress state, strain rate and temperature. They have formulated anisotropic strain rate and temperature dependent constitutive models, which can be applied to other materials with high accuracy.

Besides the ordinary thermal softening phenomena, another type of thermal effects, DSA, is also observed in many metallic materials, such as steels (Lee et al., 2011; Li et al., 2019; Wang et al., 2017; Wesselmecking et al., 2018; Yang et al., 2018), aluminum alloys (Aboulfadl et al., 2015; Benallal et al., 2008; Kreyca and Kozeschnik, 2018), Ni-Co based alloys (Cui et al., 2011), titanium alloys (Cheng and Nemat-Nasser, 2000), high-entropy alloys (Otto et al., 2013; Tsai et al., 2019), and molybdenum alloys (Cheng et al., 2001). Several phenomena including i) the Portevin–Le Chatelier (PLC) effects with serrated flow stress, ii) the increase of strength at elevated temperatures, and iii) the negative strain rate sensitivity, are typical manifestations of the DSA effect. The mechanism of DSA is mainly attributed to the dynamic interaction between the solute atoms (interstitial or substitutional) in the matrix and the mobile dislocations (McCormick, 1988; Mogucheva et al., 2016; Picu, 2004; Wang et al., 2015; Yang et al., 2018; Yuzbekova et al., 2017). Systematic experimental investigations on the thermal affected tensile properties of various metallic materials performed by Nemat-Nasser and his co-workers (Guo and Nemat-Nasser, 2006; Nemat-Nasser and Guo, 2003, 2005; Nemat-Nasser et al., 1999) have

revealed that the corresponding characteristic temperature value, where the maximum DSA intensity is reached, is influenced by both the strain rate and plastic strain. Meng and Guo (2011) and Guo and Gao (2013) have quantified the effects of temperature as well as strain rate on the intensity of the DSA in several alloys. Based on these observations, the corresponding physical-based (PB) framework has been established (Nemat-Nasser and Guo, 2003; Nemat-Nasser et al., 2001) and improved (Guo and Gao, 2013; Lee and Lee, 2012; Wang et al., 2015) to capture the non-monotonic temperature effects on the flow behavior due to the activation of the DSA mechanism in different materials. There are several other models developed to describe the DSA effects based on the physical mechanism approach as well (Gilat and Wu, 1997; Kreyca and Kozeschnik, 2018). Besides the development of analytical constitutive models, Li et al. (2019) have also applied the machine-learning approach to describe the non-monotonic temperature dependence of flow behavior in dual-phase (DP) steels and achieved high accuracy.

In view of these proposed models describing the DSA effects, all of them only consider the influence of temperature on plastic flow with respect to plastic strain and strain rates. However, a very important factor, which is the temperature effect on plastic anisotropy, is so far overlooked in the literature. Although models proposed by Khan and his co-workers (Habib et al., 2017; Khan and Baig, 2011; Khan et al., 2007; Khan and Liu, 2012; Khan and Yu, 2012; Khan et al., 2012) could account for the temperature-dependent anisotropy, the validity is not general and only limited to the thermal softening region. A universal model that could accurately capture the anisotropy evolution with respect to plastic strain and loading temperature at the same time is still missing. Therefore, the aim of the present work is to develop a generalized evolving plasticity model accurately describing the anisotropic flow behavior under the influence of temperature for both thermal softening and DSA mechanisms. We target a simple formulation and straightforward calibration procedure without numerical iteration involved, yet very high

accuracy in a large range of temperature and deformation. For this reason, the formulation is based on the evolving non-associated Hill48 model developed by Lian et al. (2018b) and the enrichment of it is detailed in section 4. Prior to the model formulation, a comprehensive experimental characterization has been conducted to evaluate the thermal effects on anisotropy across an extremely large range of temperature from -150 °C to 500 °C for two high-strength low-alloyed pipeline steels. It is noted that in the current study only quasi-static loading condition is explored. The experimental procedure and results are presented in section 2 and 3, respectively. With the obtained data for two steels, that show different responses to the temperature variation, the proposed evolving plasticity model is calibrated and validated in section 5. Further discussion on the coupling of anisotropy with temperature dependence is provided in section 6.

## 2 Materials and experimental procedures

### 2.1 Materials

In this study, two types of API X70 pipeline steel as strips with different thicknesses are used. With similar chemical composition in both materials, different thermal-mechanical parameters were applied to the hot rolling and heat treatment process of the production of these two steels. For the reason of convenience, the steel with the final strip thickness of 22 mm is referred to as X70-A and the other one with a thickness of 14 mm is referred to as X70-B. Thin sheets with a thickness of 2 mm have been cut from the plates at the position corresponding to the 1/3 thickness, from which tensile specimens have been manufactured. The microstructure of both X70 steels has been characterized after the standard sample preparation procedure using a scanning electron microscope (SEM). The microstructure shown in Figure 1 is taken from the normal surface of thin sheets. Both materials show mainly bainitic structures and some ferritic constituents. The detailed and systematic characterization of microstructure to reveal the possible underlying different deformation mechanisms is beyond the scope of this study, which is focused on the mechanical properties and corresponding constitutive models.

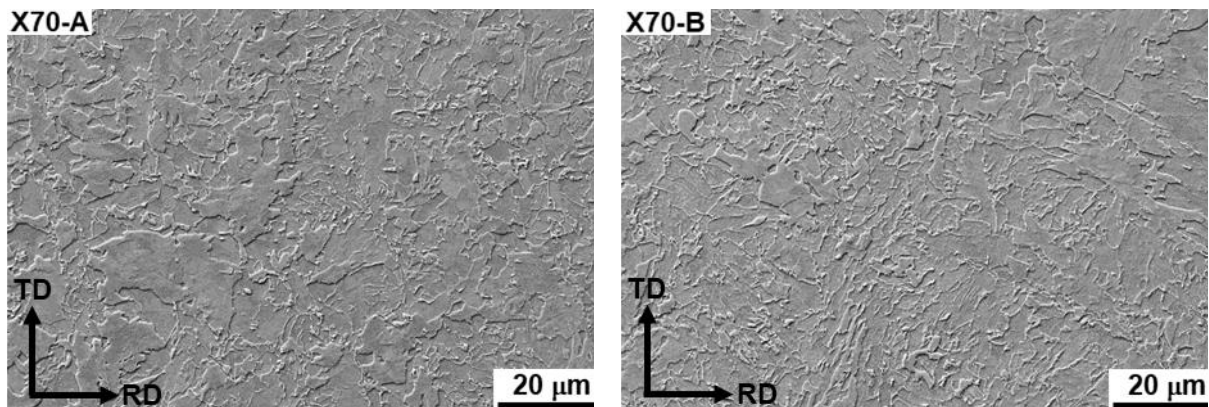


Figure 1: The microstructure of X70 steel from SEM.

### 2.2 Tensile tests at room temperature

The uniaxial tensile tests with flat smooth dog bone specimens were conducted at room

temperature (RT) according to the DIN EN ISO 6892-1 standard. In order to characterize the anisotropy effects, tests along three loading directions (0°, 45°, and 90° with respect to the rolling direction) were performed. During tensile deformation at RT using the Zwick machine Z100, one optical extensometer was applied for the measurement of the longitudinal strain and the transverse strain was measured by tracking the change of width of specimens with the assistance of one optical camera. The gauge length in the longitudinal and transverse direction was 50 mm and 12.5 mm, respectively. The crosshead velocity was controlled to be 0.4 mm/min to achieve a quasi-static loading condition with the initial strain rate of approximately  $1 \times 10^{-4} \text{ s}^{-1}$ . A detailed description of the experimental setup at RT is given by Shen et al. (2018). Both the engineering stress versus strain curves and the Lankford coefficient or r-value were measured during the uniaxial tensile tests for three different orientations at RT.

### **2.3 Tensile tests at various temperatures**

Besides RT, uniaxial tensile tests were conducted at nine additional temperatures (123, 173, 253, 273, 373, 473, 573, 673 and 773 K) using a Zwick machine Z250 following DIN EN ISO 6892-2/3 standards. Different temperatures in the thermal chamber were achieved by cooling with liquid nitrogen or induction heating, respectively. During the tensile tests, a thermocouple was attached next to the specimen to ensure the desired temperature was maintained. The same strain rate was applied to all the experiments. At these temperatures, tests were performed along the same three directions (0°, 45°, and 90°) and only one extensometer along the length direction was applied to measure the longitudinal strain. The missing measurement of the transverse strain is due to limitations in the experimental facilities when thermal chambers are used. For each testing condition, at least two parallel experiments have been carried out and very good repeatability is achieved in the obtained engineering stress–strain curves.

### 3 Experimental results

#### 3.1 Anisotropy at room temperature

The experimental flow curves at RT until the ultimate tensile strength (UTS) along three loading directions are shown in Figure 2 (a) and (b) for X70-A and X70-B, respectively. The history of r-value, defined as the plastic strain rate ratio between the width and thickness directions  $r = \dot{\epsilon}_w^p / \dot{\epsilon}_t^p$ , over the true strain along three loading angles is also depicted in Figure 2 (c) and (d) for X70-A and X70-B. The scatter from three parallel tests is calculated as well. Evident anisotropic plastic flow directionality is observed in both materials. The anisotropy patterns of the stress are quite different in these two materials. The highest flow stress is observed along the transverse direction (TD), i.e. 90° among these three loading directions in both materials. The lowest flow stress is along the rolling direction (RD), i.e. 0° in X70-A and that of X70-B appears along the diagonal direction (DD), i.e. 45°. The r-value is the highest along the DD and the lowest along the RD in both materials. It is also obvious that the r-values along different loading directions are evolving during plastic deformation.

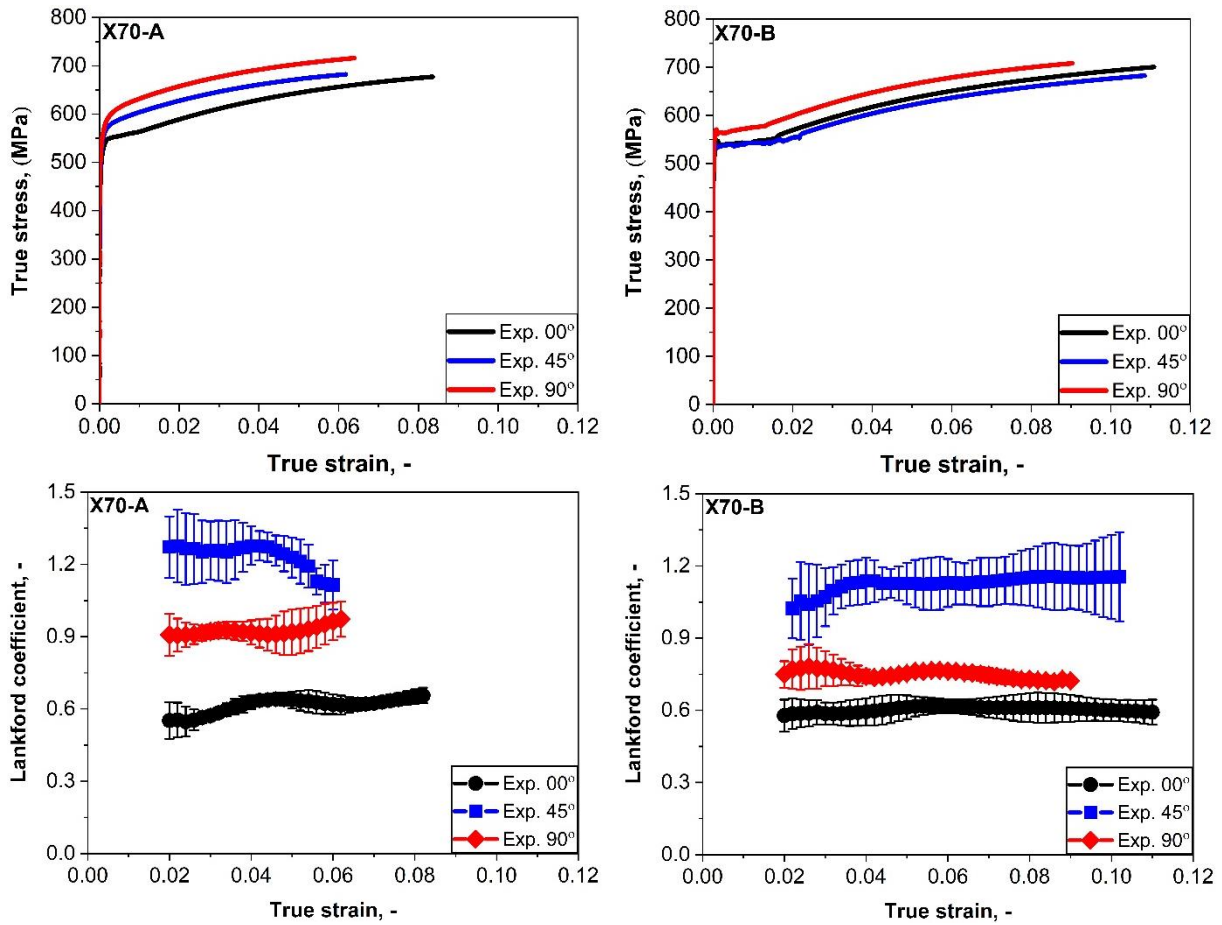


Figure 2: The uniaxial tensile properties along three loading directions of 0°, 45° and 90° at room temperature for two high-strength steels.

### 3.2 Thermal effects on anisotropy

The true stress–strain curves until the corresponding UTS obtained at temperatures below RT along three loading directions for both materials are shown in Figure 3. It is obvious for both materials along three loading directions, higher flow stress is observed with the decrease of temperature from RT, which is related to the typical thermal softening effects. In general, the uniform strain values are also increased by decreasing temperature, which is related to the complicated microstructure and deformation mechanisms of bainitic steels. Further investigations are necessary to reveal the underlying mechanisms.

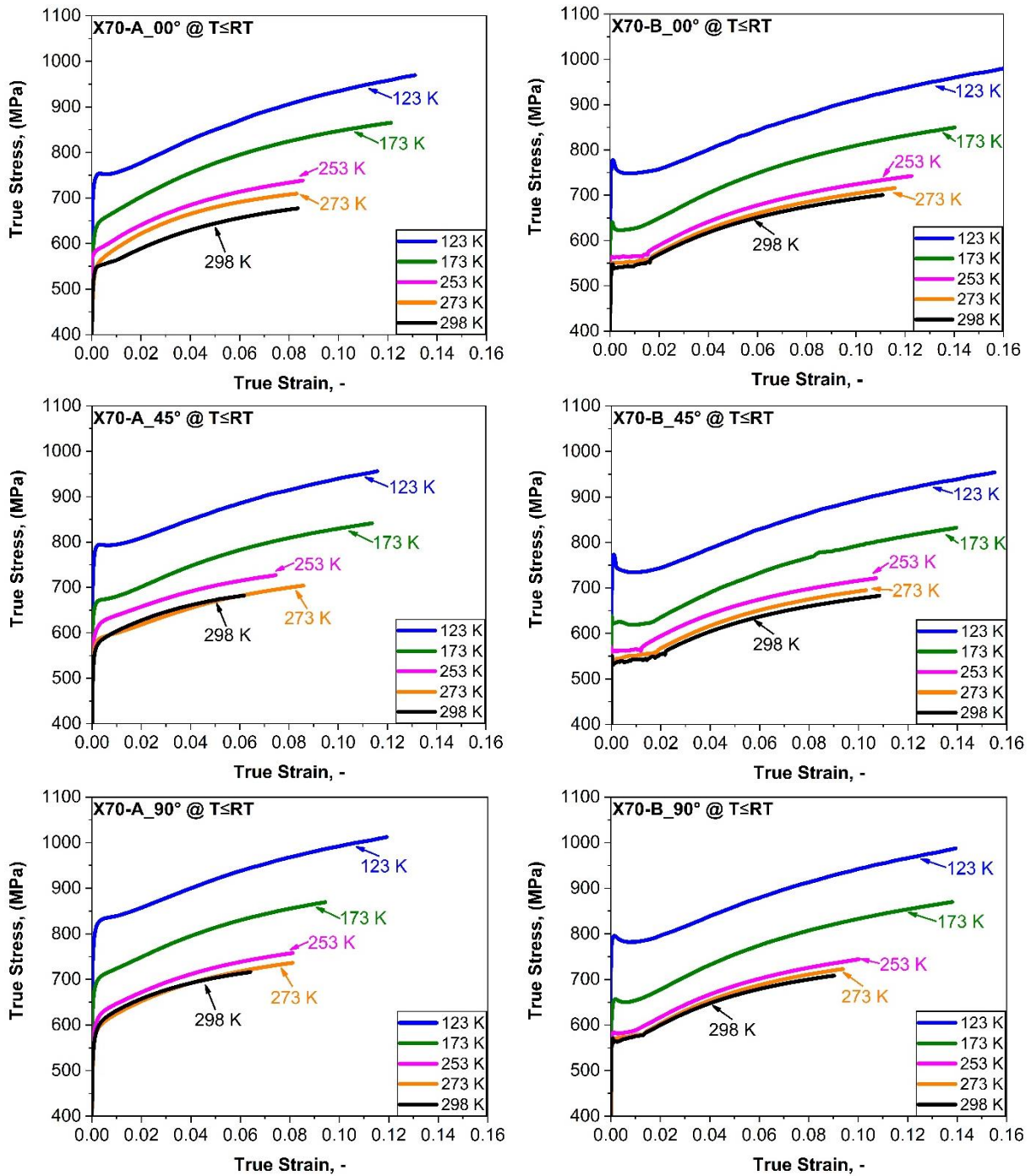


Figure 3: The true stress–strain curves at temperatures below RT along three loading angles for both materials.

The experimental true stress–strain curves until the corresponding UTS obtained at temperatures above RT along three loading directions for both materials are shown as solid curves in Figure 4.

From these results, it is easily recognized that the strength of both materials is following a non-monotonic trend with the increase of temperature. In general, the strength is firstly increased to

a peak value at the temperature of 573 K and then decreased with a further increase of temperature. In material X70-A, serrated flow stress is observed along the three directions at 473 K. In contrast, staircase-type flow curves are noticed in X70-B at 473 K along the three loading directions. The different manifestations of the DSA on the flow curves of these two steels are typically related to the distinct microstructures, which affect the dynamics of the nucleation and propagation of deformation bands as detailed in several recent studies (Mogucheva et al., 2016; Yuzbekova et al., 2017; Zhemchuzhnikova et al., 2017; Zhemchuzhnikova et al., 2018). It should be mentioned that only the global flow behavior in terms of stress–strain curves is considered in this study though strain localization is accompanied by the jerky flow at 473 K. There have been numerous investigations conducted to reveal the mechanisms of the DSA, which is generally understood as the dynamic interaction between the mobile dislocations and solute atoms, such as C and N in different types of steels (Lee et al., 2011; Wang et al., 2017; Wesselmecking et al., 2018; Yang et al., 2018), and Mg in Al-Mg based alloys (Cai et al., 2017; Kreyca and Kozeschnik, 2018; Picu, 2004; Picu and Zhang, 2004), under certain loading conditions. As the diffusivity of solute atoms and the mobility of dislocations are promoted by temperature increase to different degrees, the maximum intensity of the DSA occurs under a specific combination of strain rate and temperature.

Table 1 Calibrated parameters in hardening functions for the flow curve extrapolation at 773 K.

Constants	$\sigma = w \cdot \sigma_{\text{Swift}} + (1 - w) \cdot \sigma_{\text{Voce}} \quad (w=0.5)$					
	$\sigma_{\text{Swift}} = A \cdot (\varepsilon_0 + \bar{\varepsilon}^p)^n$			$\sigma_{\text{Voce}} = k_0 + Q \cdot (1 - \exp(-\beta \cdot \bar{\varepsilon}^p))$		
	$A$	$\varepsilon_0$	$n$	$k_0$	$Q$	$\beta$
X70-A_00°	873.4	0.001	0.076	230.0	120.7	379.1
X70-A_45°	710.7	0.001	0.077	350.0	122.0	471.2
X70-A_90°	816.2	0.001	0.066	250.0	164.6	632.7
X70-B_00°	569.6	0.001	0.056	351.7	71.85	144.5
X70-B_45°	689.5	0.010	0.060	221.9	92.54	172.4
X70-B_90°	580.0	0.001	0.050	331.8	109.6	214.6

It is noticed that temperature has pronounced influence on both flow stress and uniform strain. The uniform strain is drastically reduced at 773 K in both materials. At most temperatures, the uniform strain values are larger than 0.06 in material X70-A and that minimum value is approximately 0.08 in material X70-B. In order to describe the thermal affected flow behavior over a wide strain range, the flow curves at 773 K have been extrapolated using a combined Swift-Voce hardening law to the strain value of 0.06 for X70-A and 0.08 for X70-B. The extrapolated flow curves at 773 K are represented by dotted curves in Figure 4 and the calibrated parameters in the hardening equations are summarized in Table 1 for both materials.

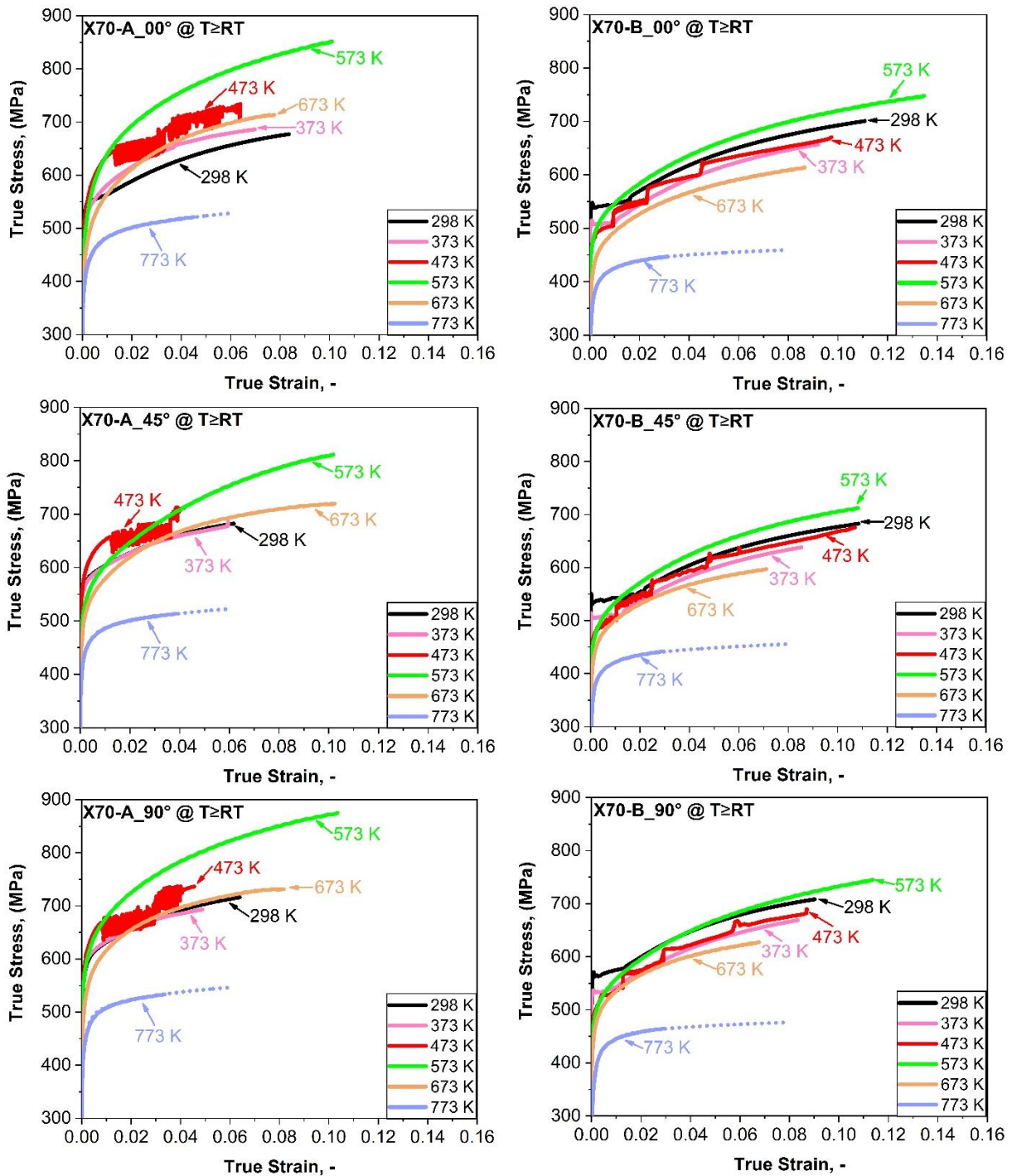


Figure 4: The true stress–strain curves at temperatures above RT along three loading angles for both materials.

In order to quantitatively characterize the thermal effects on the flow behavior of the investigated materials, the normalized strength has been used as an evaluation variable. The normalized strength is calculated as the ratio between the true stress at different temperatures over the

reference stress at RT along the corresponding loading direction at the same strain level. For the consideration of the evolving features of thermal effects, the normalized strength has been calculated at three representative strain levels for all three loading directions and plotted in Figure 5. In order to cover the complete uniform deformation range, three true strain values, i.e. 0.002, 0.04 and 0.06 have been selected for X70-A and the strain values of 0.002, 0.04 and 0.08 have been selected for X70-B. It is observed that the intensity of the DSA is not only influenced by temperature but also by the plastic strain level. For example, in material X70-A the most pronounced DSA at the yield point occurs at 473 K and with the increase of plastic strain it shifts to 573 K at the strain level of 0.04. In material X70-B, the influence of the DSA on the yield strength is not pronounced but it is enhanced as the strain level increases. One possible explanation is that with increasing plastic deformation, more dislocations are generated and the dynamic interaction between solute atoms and mobile dislocations is enhanced, leading to the more pronounced DSA effects (Picu, 2004). Though the dynamic interaction between solute atoms and dislocations takes place from the beginning of plastic deformation, it has been reported by several researchers that a critical incubation strain is necessary for the DSA to produce significant effects, e.g. the onset of the PLC effect, in different alloys (Kobeleev et al., 2017; Kubin and Estrin, 1990, 1992; Mazière and Dierke, 2012). These observations indicate the importance of the strain dependence for the accurate description of the DSA related phenomena.

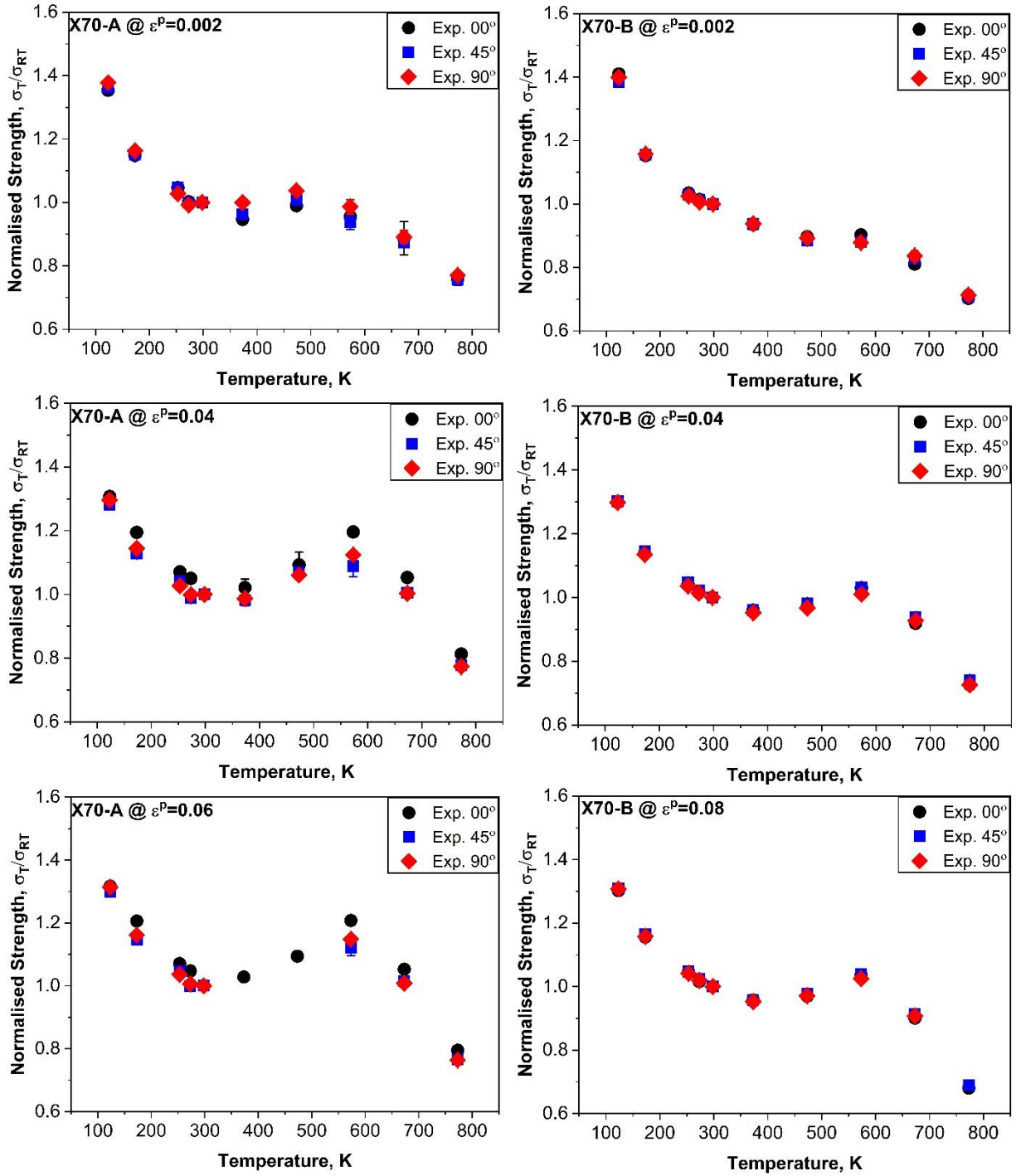


Figure 5: The distribution of normalized strength over temperature determined from uniaxial tensile tests along three loading directions at different plastic strain levels.

For the consideration of anisotropic hardening, we have made the work equivalence transformation on the obtained experimental results, which is explained in our previous publication (Lian et al., 2018b) and shown in Figure 6. The flow curve of the tensile test along

the rolling direction is taken as the reference and the work equivalence principle has been applied to the flow curve along the  $\theta$  direction. At the same amount of plastic work along different loading directions, i.e. with the identical integral area until  $(\varepsilon_\theta, \sigma_\theta)$  and  $(\varepsilon_0, \sigma_0)$ , a new pair of stress and strain data (PEEQ,  $\sigma_\theta$ ) is constructed as the work-equivalent conjugated result. By using this approach, the experimental equivalent plastic strain (PEEQ) is correlated with the plastic work and independent of the definition of the yield function and strain potential. This work equivalence transformation can also be applied to other biaxial or multi-axial loading conditions. Therefore, for the description of the yield locus evolution and anisotropic stress distribution, the PEEQ instead of the true plastic strain along corresponding loading direction is applied in this study.

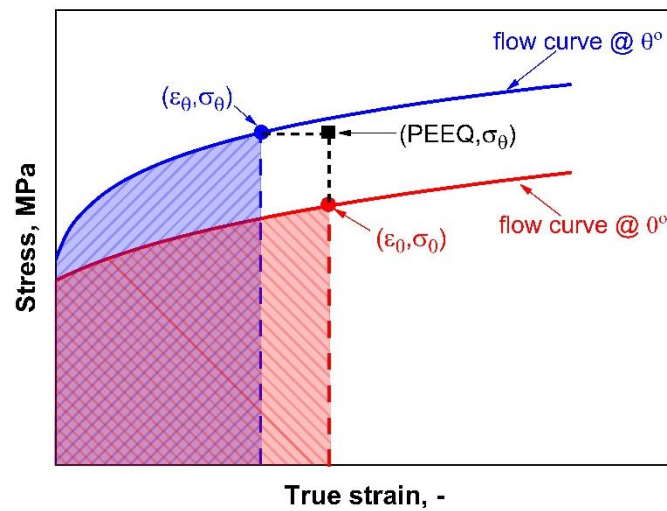


Figure 6: The schematic demonstration of the work equivalence principle, modified from Lian et al. (2018b).

In addition, it is also noticed that the anisotropy pattern of the investigated materials is affected by temperature in a quite different way. For a quantitative description of the anisotropic stress directionality, the normalized stress  $\sigma_N$  is applied. In this case, the flow stress along different loading directions  $\sigma_\theta$  is normalized by the corresponding stress at the same value of the PEEQ along the RD  $\sigma_0$  ( $\sigma_N = \sigma_\theta / \sigma_0$ ). For better visualization of the thermal effects on anisotropy, the normalized stress  $\sigma_N$  obtained at different temperatures at the same strain level (PEEQ=0.04)

has been plotted over the loading direction in Figure 7. It is obvious that the anisotropy patterns in the stress distribution of these two materials are affected by temperature to very distinct degrees. For material X70-A, the temperature has pronounced effects on the anisotropic behavior as the relative strength along three loading directions varies significantly with temperature. For material X70-B, no evident temperature effects on anisotropy can be recognized, especially when the temperature is below RT.

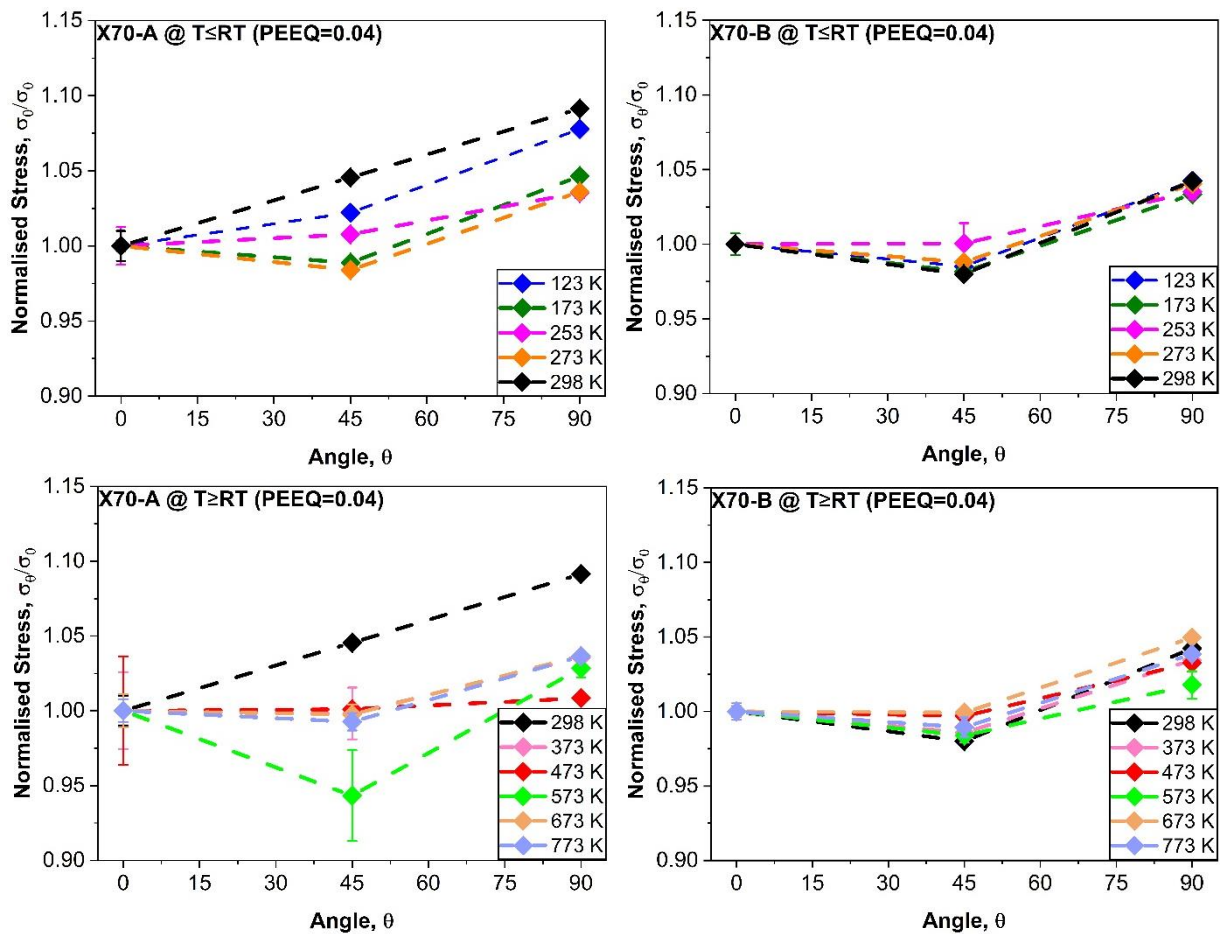


Figure 7: The influence of temperature on the distribution of the normalized stress over the loading direction at the equivalent plastic strain of 0.04.

In this study, experimental flow stress under the equibiaxial tension condition at different temperatures is not available and it is determined as the average value of flow stress from three uniaxial tensile tests, calculated as  $\sigma_b = (\sigma_0 + 2 \times \sigma_{45} + \sigma_{90})/4$  according to Park et al. (2019a) and Zhang et al. (2017). Combining the results from three uniaxial tensile tests and the

equibiaxial tensile stress, the yield locus can be constructed at different temperatures and strain levels, which provides an overview of the plastic behavior. The yield locus at five representative temperatures predicted by the developed evolving plasticity model in this study is depicted in Figure 8, where the experimental results from the uniaxial as well as equibiaxial tensile stresses are represented by different symbols. The results at the equivalent plastic strain value of 0.04 are taken as examples to reveal the thermal effects on anisotropy for both materials. It is obvious the thermal impacts on the yield locus are more pronounced in X70-A than X70-B. From the experimental observation, it is concluded that the temperature has anisotropic effects in X70-A while its influence is almost isotropic in X70-B. The underlying reasons and mechanisms for such complicated thermals effects on anisotropy need further investigations.

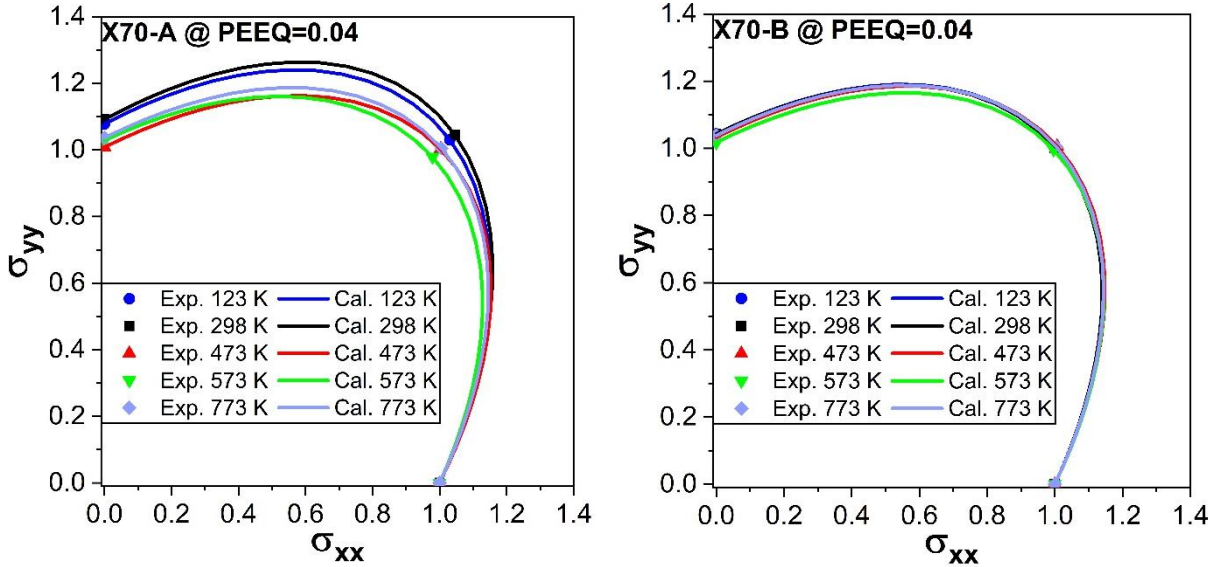


Figure 8: The prediction of the yield locus at the equivalent plastic strain of 0.04 in comparison with experimental results at five representative temperatures.

## 4 Constitutive model

### 4.1 Evolving anisotropic plasticity model

In order to overcome the inaccuracy in simultaneously describing the anisotropy of stress and r-value using the conventional Hill48 model (Hill, 1948), the non-associated Hill48 (nHill48) model has been proposed (Stoughton, 2002) through the combination of the non-associated flow rule. While pursuing the further improvement of accuracy considering the microstructure evolution, the evolving non-associated Hill48 (enHill48) model is developed by Lian et al. (2018b), which is also referred to as evolving plasticity (EP2018) model in this study. The key functions describing the yield function  $f$ , flow potential  $g$  and flow rule are summarized as:

$$f = \bar{\sigma}(\alpha_{i\sim j}, \boldsymbol{\sigma}) - \sigma_Y(\bar{\epsilon}^p) \leq 0 \quad \text{Eq. 1}$$

$$g = \bar{\sigma}(\beta_{i\sim j}, \boldsymbol{\sigma}) - \sigma_Y(\bar{\epsilon}^p) \leq 0 \quad \text{Eq. 2}$$

$$\dot{\boldsymbol{\epsilon}}^p = \dot{\lambda} \cdot \frac{\partial g}{\partial \boldsymbol{\sigma}} \quad \text{Eq. 3}$$

where  $\bar{\sigma}$  is the equivalent stress with  $\alpha_{i\sim j}$  and  $\beta_{i\sim j}$  as anisotropic parameters that correlate the response of the material under arbitrary loading conditions defined by the stress tensor  $\boldsymbol{\sigma}$  with the reference stress state  $\sigma_Y(\bar{\epsilon}^p)$ .  $\dot{\lambda}$  is a scalar factor with non-negative values used for updating the plastic strain rate tensor  $\dot{\boldsymbol{\epsilon}}^p$ .

As a simple quadratic expression capable of describing the three-dimensional anisotropy with reasonable accuracy, the Hill48 equivalent stress is expressed as:

$$\bar{\sigma}(\alpha_{i\sim j}, \boldsymbol{\sigma}) = \left\{ \frac{1}{2} [F_\sigma(\sigma_{22} - \sigma_{33})^2 + G_\sigma(\sigma_{33} - \sigma_{11})^2 + H_\sigma(\sigma_{11} - \sigma_{22})^2] + L_\sigma \sigma_{23}^2 + M_\sigma \sigma_{13}^2 + N_\sigma \sigma_{12}^2 \right\}^{\frac{1}{2}} \quad \text{Eq. 4}$$

$$\bar{\sigma}(\beta_{i\sim j}, \boldsymbol{\sigma}) = \left\{ \frac{1}{2} [F_r(\sigma_{22} - \sigma_{33})^2 + G_r(\sigma_{33} - \sigma_{11})^2 + H_r(\sigma_{11} - \sigma_{22})^2] + L_r \sigma_{23}^2 + M_r \sigma_{13}^2 + N_r \sigma_{12}^2 \right\}^{\frac{1}{2}} \quad \text{Eq. 5}$$

where  $F_\sigma$ ,  $G_\sigma$ ,  $H_\sigma$ ,  $L_\sigma$ ,  $M_\sigma$  and  $N_\sigma$  correspond to anisotropic parameters ( $\alpha_{1\sim 6}$ ) in the yield function while  $F_r$ ,  $G_r$ ,  $H_r$ ,  $L_r$ ,  $M_r$  and  $N_r$  represent anisotropic parameters ( $\beta_{1\sim 6}$ ) in the flow

potential, which are calibrated independently using experimental results obtained from uniaxial and biaxial tensile tests. The calibration of these parameters for the yield function and flow potential ( $L = M = 3$  for plane stress condition) is given in the following equations.

$$\begin{aligned}
F_{\sigma} &= \frac{\sigma_0^2(\bar{\epsilon}^P)}{\sigma_{90}^2(\bar{\epsilon}^P)} - 1 + \frac{\sigma_0^2(\bar{\epsilon}^P)}{\sigma_b^2(\bar{\epsilon}^P)} & F_r &= \frac{2r_0(\bar{\epsilon}^P)}{r_{90}(\bar{\epsilon}^P)(1+r_0(\bar{\epsilon}^P))} \\
G_{\sigma} &= 1 - \frac{\sigma_0^2(\bar{\epsilon}^P)}{\sigma_{90}^2(\bar{\epsilon}^P)} + \frac{\sigma_0^2(\bar{\epsilon}^P)}{\sigma_b^2(\bar{\epsilon}^P)} & G_r &= \frac{2}{1+r_0(\bar{\epsilon}^P)} \\
H_{\sigma} &= 1 + \frac{\sigma_0^2(\bar{\epsilon}^P)}{\sigma_{90}^2(\bar{\epsilon}^P)} - \frac{\sigma_0^2(\bar{\epsilon}^P)}{\sigma_b^2(\bar{\epsilon}^P)} & H_r &= \frac{2r_0(\bar{\epsilon}^P)}{1+r_0(\bar{\epsilon}^P)} \\
N_{\sigma} &= \frac{4\sigma_0^2(\bar{\epsilon}^P)}{\sigma_{45}^2(\bar{\epsilon}^P)} - \frac{\sigma_0^2(\bar{\epsilon}^P)}{\sigma_b^2(\bar{\epsilon}^P)} & N_r &= \frac{(r_{90}(\bar{\epsilon}^P)+r_0(\bar{\epsilon}^P))(1+2r_{45}(\bar{\epsilon}^P))}{r_{90}(\bar{\epsilon}^P)(1+r_0(\bar{\epsilon}^P))}
\end{aligned} \tag{Eq. 6}$$

where  $\sigma_0$ ,  $\sigma_{45}$ ,  $\sigma_{90}$ , and  $\sigma_b$  represent the flow stress for uniaxial tensile tests along RD, DD, TD, and the equibiaxial tensile test.  $r_0$ ,  $r_{45}$  and  $r_{90}$  are the r-values for uniaxial tensile tests along RD, DD, and TD. To capture the evolving anisotropy in terms of anisotropic hardening and r-value evolution, the flow stress and the r-values along different directions are taken as functions of the plastic deformation, automatically leading to the evolution of the anisotropic parameters. It is noted that the plastic strain here is referred to as the PEEQ defined previously conjugated to the plastic work, instead of the true plastic strain obtained directly from the tensile tests. It is necessary to use it to make sure the definition of equivalent strain independent of the choice of the constitutive equations.

## 4.2 Thermal-dependent evolving anisotropic model

To address the thermal effects, the temperature function  $f(T)$ , i.e. the normalized strength is adopted to quantify the influence of temperature on the flow behavior.

$$f = \bar{\sigma}(\alpha_{i \sim j}, \boldsymbol{\sigma}) - f(T) \cdot \sigma_{\text{ref}}(\bar{\epsilon}^P) \leq 0 \tag{Eq. 7}$$

$$g = \bar{\sigma}(\beta_{i \sim j}, \boldsymbol{\sigma}) - f(T) \cdot \sigma_{\text{ref}}(\bar{\epsilon}^P) \leq 0 \tag{Eq. 8}$$

$$f(T) = \frac{\sigma_T}{\sigma_{\text{ref}}} \quad \text{Eq. 9}$$

The flow stress at RT is selected as the reference stress. Both thermal softening and DSA are exhibited at different temperatures in the investigated materials. Therefore, a thermal-dependent model capable of capturing both aspects is of crucial importance. The additive decomposition of the temperature effects into the thermal softening component and the DSA component is applied in this study.

$$f(T) = f_{\text{TS}}(T) + f_{\text{DSA}}(T) \quad \text{Eq. 10}$$

The first term  $f_{\text{TS}}(T)$  is related to the thermal softening behavior while the second term  $f_{\text{DSA}}(T)$  quantifies the contribution from the DSA.

#### **4.2.1 Thermal softening model**

The macroscopic thermal softening effects are typically related to the temperature-dependent dislocation behavior at the microscopic scale in metallic materials. In general, the easier for dislocations to overcome certain obstacles, the softer the materials behave. There are two types of obstacles to the dislocation motion, one is the long-range barrier and the other one is the short-range barrier (Reed, 1972; Wang et al., 2015). Typical long-range barriers are difficult to overcome by thermal activation. Therefore, the contribution to the flow stress from these barriers shows marginal temperature dependence and can be treated as the athermal component. In contrast, short-range barriers can be relatively easily overcome through the assistance of thermal activation and these barriers contribute to the majority of the temperature-dependent components of the flow stress. Forest dislocations, point defects (vacancies and solute atoms) and Peierls stress are typical short-range barriers in metallic materials (Wang et al., 2015). There are several models available for the description of the thermal softening effects on the flow behavior, such as the JC model, the KHL model, the PB model, and the ZA model. In this study, a simple

phenomenological Arrhenius type model is adopted to describe the thermal activation related materials behavior, as it has been used in several previous studies (Liu et al., 2020; Muenstermann et al., 2013; Novokshanov et al., 2015). The contribution from the thermal softening related phenomena to the total thermal effects on the flow stress can be expressed as:

$$f_{TS}(T) = C_1 \cdot \exp(-C_2 \cdot T) + C_3 \quad \text{Eq. 11}$$

where  $C_{1\sim3}$  are material parameters.  $C_1$  and  $C_2$  are related to the thermal activation components and  $C_3$  generally describes the athermal contribution.

#### **4.2.2 Dynamic strain aging model**

The DSA phenomena have been observed in various materials under certain deformation conditions. Due to the existence of the DSA, some abnormal behavior can be observed, such as the serrated flow stress, the increase of flow stress with temperature, the negative strain rate sensitivity and significantly reduced ductility (Wang et al., 2015; Yang et al., 2018). The dynamic interaction between interstitial (C or N in steels) and/or substitutional (Mg in Al-Mg alloys) solute atoms with mobile dislocations has been generally accepted as the underlying reason for the occurrence of the DSA (McCormick, 1988). Under certain loading conditions within the specific range of strain rate and temperature, these solute atoms have sufficient diffusivity to encircle the dislocations cores, thereby introducing an additional resistance to mobile dislocations. The increase of deformation temperature can enhance both the diffusion of solute atoms and the mobility of dislocations. Once the combination of strain rate, temperature, and plastic strain meets the specific condition, the diffusion rate of solute atoms and the motion of dislocations reach such a balance that the intensity of the DSA reaches its maximum. Under a specific loading rate, the pinning effects of solute atoms on dislocation motion are weakened when the temperature is further increased beyond the characteristic temperature, at which the peak intensity of the DSA occurs, leading to a bell-shaped distribution of flow stress over

temperature. Most of the physical-based models (Böhlke et al., 2009; Mazière and Dierke, 2012) that have been proposed to represent the DSA mechanisms as well as to predict the DSA phenomena are only available for RT loading condition. There are also several phenomenological models available for the description of the DSA effects for varied loading temperatures and strain rates (Guo and Gao, 2013; Hong, 1985; Lee and Lee, 2012; Shen et al., 2019a; Wang et al., 2015). However, in these models, the DSA effects have been evaluated only at discrete points, such as yielding point or specific strain values. In addition, these phenomenological models are restricted to isotropic materials, and the dynamic interaction between DSA and anisotropy has not been considered so far. Therefore, it is the aim of the current study to strengthen the phenomenological models with an evolving description of the general thermal effects in an anisotropic framework. In terms of formulation, the anisotropy will be reflected in the yield function definition, while the contribution from the DSA phenomena to the total thermal effects on the flow stress can be expressed as a symmetric bell-shaped function of temperature:

$$f_{\text{DSA}}(T) = C_4 \cdot \exp \left[ - \left( \frac{T - C_5}{C_6} \right)^2 \right] \quad \text{Eq. 12}$$

where  $C_{4\sim 6}$  are material parameters, which need to be calibrated.  $C_4$  and  $C_6$  are related to the intensity of the DSA and  $C_5$  describes the corresponding characteristic temperature with the most intensive DSA at a certain strain level and strain rate.

#### 4.2.3 Evolving plasticity model considering anisotropic thermal dependence

The material properties in terms of anisotropy and thermal effects show a clear dependence on the plastic strain according to the experimental results. Due to texture evolution as well as the increasing dislocation density, the interaction between solute atoms and mobile dislocations is also changing during plastic deformation. Therefore, the evolving aspects of anisotropy, as well as thermal effects, should not be overlooked, especially when the mechanism of DSA is activated. In order to capture the evolving features of plasticity, a straightforward modification has been

made by making all material parameters in the thermal-dependent model evolve with the plastic strain  $\bar{\varepsilon}^p$ . A generalized formula, which is a combination of exponential and polynomial functions, is proposed to describe the strain dependence of thermal parameters.

$$C_{i=1\sim 6} = \sum_{j=0}^j P_i^j \cdot (\bar{\varepsilon}^p)^j + Q_i^1 \cdot \exp(-Q_i^2 \cdot \bar{\varepsilon}^p) \quad \text{Eq. 13}$$

where  $C_{i=1\sim 6}$  are thermal parameters describing the thermal softening and the DSA effects.

$P_i^{0\sim j}$  and  $Q_i^{1\sim 2}$  are parameters used to describe the evolution of individual thermal parameters.

In combination with the thermal-dependent model, a generalized evolving plasticity (EP2019) model is proposed based on the anisotropic non-associated Hill48 model, which can be used to simultaneously predict the directionality of stress and r-value under the influence of temperature.

In summary, the three major constituents including the yield function, the flow potential and the temperature function in the generalized constitutive model that is capable of describing the evolving anisotropy, thermal softening and dynamic strain aging effects are expressed as:

$$f = \bar{\sigma}(F_\sigma, G_\sigma, H_\sigma, L_\sigma, M_\sigma, N_\sigma, \boldsymbol{\sigma}) - \sigma_{\text{ref}}(\bar{\varepsilon}^p) \cdot f(T, \bar{\varepsilon}^p) \leq 0 \quad \text{Eq. 14}$$

$$g = \bar{\sigma}(F_r, G_r, H_r, L_r, M_r, N_r, \boldsymbol{\sigma}) - \sigma_{\text{ref}}(\bar{\varepsilon}^p) \cdot f(T, \bar{\varepsilon}^p) \leq 0 \quad \text{Eq. 15}$$

$$f(T, \bar{\varepsilon}^p) = C_1(\bar{\varepsilon}^p) \cdot \exp(-C_2(\bar{\varepsilon}^p) \cdot T) + C_3(\bar{\varepsilon}^p) + C_4(\bar{\varepsilon}^p) \cdot \exp\left[-\left(\frac{T-C_5(\bar{\varepsilon}^p)}{C_6(\bar{\varepsilon}^p)}\right)^2\right] \quad \text{Eq. 16}$$

$F_{\sigma/r}$ ,  $G_{\sigma/r}$ ,  $H_{\sigma/r}$ ,  $L_{\sigma/r}$ ,  $M_{\sigma/r}$  and  $N_{\sigma/r}$  are anisotropic parameters and  $C_{1\sim 6}$  are thermal related material parameters. In the case of plane stress condition, the anisotropic parameters of  $L_{\sigma/r}$  and  $M_{\sigma/r}$  are typically assumed to be three and other parameters need to be calibrated based on either flow stress or r-value obtained from tensile tests.

Once the evolution of thermal material parameters is determined, the flow stress with the dependence of temperature and plastic strain can be calculated based on the flow curve along the corresponding direction at the reference temperature. The evolution of r-value at different

temperatures can be determined in a similar method. Given the evolution of flow stress and r-value along different loading directions at various temperatures, the anisotropic parameters can be explicitly calculated using either the stress method or the r-value method with the dependence of both temperature  $T$  and plastic strain  $\bar{\epsilon}^P$ .

$$\begin{aligned}
F_\sigma &= \frac{\sigma_0^2(\bar{\epsilon}^P, T)}{\sigma_{90}^2(\bar{\epsilon}^P, T)} - 1 + \frac{\sigma_0^2(\bar{\epsilon}^P, T)}{\sigma_b^2(\bar{\epsilon}^P, T)} & F_r &= \frac{2r_0(\bar{\epsilon}^P, T)}{r_{90}(\bar{\epsilon}^P, T)(1+r_0(\bar{\epsilon}^P, T))} \\
G_\sigma &= 1 - \frac{\sigma_0^2(\bar{\epsilon}^P, T)}{\sigma_{90}^2(\bar{\epsilon}^P, T)} + \frac{\sigma_0^2(\bar{\epsilon}^P, T)}{\sigma_b^2(\bar{\epsilon}^P, T)} & G_r &= \frac{2}{1+r_0(\bar{\epsilon}^P, T)} \\
H_\sigma &= 1 + \frac{\sigma_0^2(\bar{\epsilon}^P, T)}{\sigma_{90}^2(\bar{\epsilon}^P, T)} - \frac{\sigma_0^2(\bar{\epsilon}^P, T)}{\sigma_b^2(\bar{\epsilon}^P, T)} & H_r &= \frac{2r_0(\bar{\epsilon}^P, T)}{1+r_0(\bar{\epsilon}^P, T)} \\
N_\sigma &= \frac{4\sigma_0^2(\bar{\epsilon}^P, T)}{\sigma_{45}^2(\bar{\epsilon}^P, T)} - \frac{\sigma_0^2(\bar{\epsilon}^P, T)}{\sigma_b^2(\bar{\epsilon}^P, T)} & N_r &= \frac{(r_{90}(\bar{\epsilon}^P, T)+r_0(\bar{\epsilon}^P, T))(1+2r_{45}(\bar{\epsilon}^P, T))}{r_{90}(\bar{\epsilon}^P, T)(1+r_0(\bar{\epsilon}^P, T))}
\end{aligned} \tag{Eq. 17}$$

In the above equations,  $\sigma_0$ ,  $\sigma_{45}$ ,  $\sigma_{90}$ ,  $r_0$ ,  $r_{45}$  and  $r_{90}$  are flow stress and r-value from uniaxial tensile tests at different temperatures loaded along corresponding directions.  $\sigma_b$  is the flow stress under the equibiaxial tensile condition at different temperatures.

## 5 Material parameter calibration and validation

For the complete calibration and validation of all material parameters in the evolving plasticity model, three major aspects are considered and briefly summarized.

a) Plasticity parameters at RT;

This is an independent step to evaluate the accuracy of the plasticity model in describing the anisotropy at RT. The normalized stress and r-values from 0°, 45°, and 90° are used as inputs to calibrate anisotropic parameters and the validation is based on the prediction of stress and r-value distribution at RT.

b) Thermal parameter calibration and validation;

1) Calibration of thermal softening parameters  $C_{1\sim3}$ : The inputs for this step are the experimental normalized strength at temperatures outside the DSA region.

2) Determination of the DSA parameters  $C_{4\sim6}$ : The inputs for the current step are obtained by subtracting the thermal softening components from the total experimental normalized strength. The validation of thermal parameters  $C_{1\sim6}$  is based on the prediction of normalized strength over a wide range of temperatures.

3) Description of the evolution of thermal parameters. The inputs are calibrated thermal parameters at discrete strain values. The outputs from this step are calibrated parameters  $P^{0\sim j}$  and  $Q^{1\sim 2}$  describing the evolution of thermal parameters. The validation at this stage relies on the accurate prediction of flow stress over a wide range of strain and temperature.

c) Validation of thermal effects on anisotropy.

This is a final validation step of the complete evolving plasticity model. The referent flow curves at RT and the evolution functions of thermal parameters along 0°, 45° and 90° act as inputs and the yield locus as functions of temperature and strain can be calculated. The

flow stress at any temperature and strain values along any loading orientations can be predicted. The validation is accomplished based on the anisotropic distribution of normalized stress over loading orientation under the influence of temperature and strain. The calibration methodology is consistent; however, a slight difference exists regarding the work equivalence transformation in different applications. In order to directly compare with experimental flow curves, the true strain is adopted as the independent variable for the prediction of flow stress as functions of strain and temperature along three different directions. For the prediction of the continuous evolution of yield locus and anisotropic stress distribution at different temperatures, the work equivalence transformation is performed and the PEEQ is used as the independent variable in the following.

### **5.1 Anisotropic parameter calibration at RT**

When the quadratic Hill48 equivalent stress is applied, explicit descriptions for the identification of anisotropic parameters are available and summarized in our previous study (Lian et al., 2018b). It has been mentioned above that anisotropy depends on the degree of plastic deformation, therefore, the calibration of the parameters at RT in the enHill48 (EP2018) model has been performed at different levels of the PEEQ. For detailed processing of the data concerning work equivalence manipulation, the readers are referred to Lian et al. (2018b). The experimental results of the r-value and the normalized stress, averaged from three parallel tests, at different strain levels are listed in Table 2. As depicted in Figure 9, in both materials at three representative PEEQ values, the EP2018 plasticity model provides high accuracy in the prediction on the anisotropic distribution of both the normalized stress and the r-values, proving its efficiency in describing the evolving features of anisotropic plasticity at RT.

Table 2 Experimental results of the normalized stress and the r-value of X70 steel at three different values of the equivalent plastic strain at RT.

Materials	PEEQ	$\sigma_0/\sigma_0$	$\sigma_{45}/\sigma_0$	$\sigma_{90}/\sigma_0$	$\sigma_b/\sigma_0$	$r_0$	$r_{45}$	$r_{90}$
X70-A	0.002	1.00	1.04	1.07	1.04	-	-	-
	0.04	1.00	1.05	1.09	1.05	0.63	1.27	0.92
	0.06	1.00	1.03	1.08	1.04	0.62	1.13	0.93
X70-B	0.002	1.00	0.99	1.05	1.01	-	-	-
	0.04	1.00	0.98	1.04	1.00	0.59	1.14	0.74
	0.08	1.00	0.98	1.03	1.00	0.61	1.15	0.73

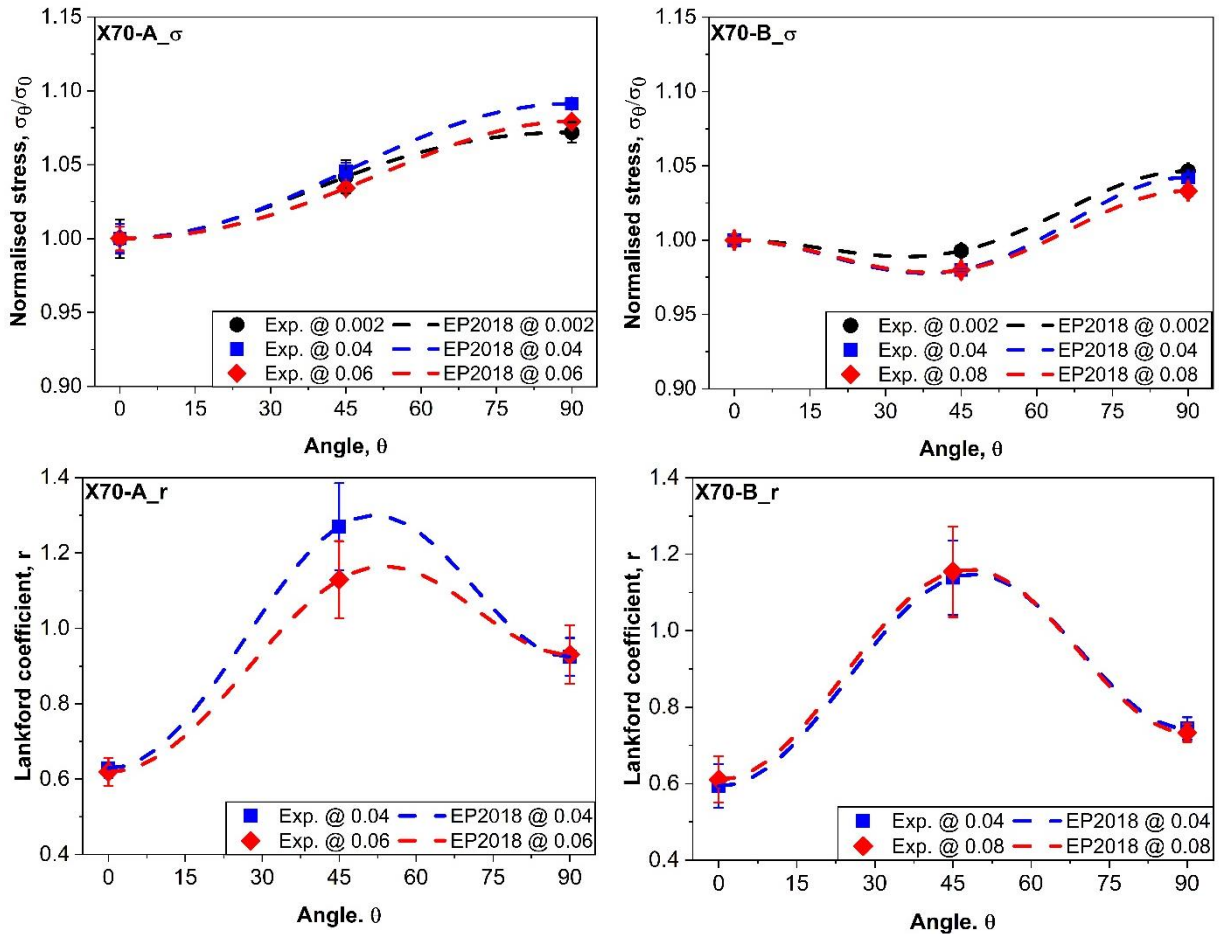


Figure 9: Predicted results of anisotropy using the enHill48 (EP2018) model at different values of the equivalent plastic strain compared with experimental results.

## 5.2 Thermal softening component calibration

As explained in the above section, the temperature effects on the flow stress can be additively decomposed into the thermal softening component and the DSA component. To quantitatively evaluate the thermal dependence of flow stress, the normalized strength has been calculated at different strain levels for 0°, 45°, and 90° loading directions. For the reason of consistency, the same three representative plastic strain values are taken as examples for the thermal parameters calibration and the corresponding results are depicted in Figure 10. The dynamic strain aging usually takes place within a specific temperature range under the quasi-static loading condition in steels, which is approximately between 350 K and 700 K. Therefore, the experimental results below RT and the results at the highest temperature (773 K in this study) are used for the calibration of parameters  $C_{1\sim3}$  in the thermal softening model. With all the calibrated parameters according to Eq. 11 at three corresponding plastic strain levels and loading orientations, it is clear that accurate description of normalized strength is achieved at low temperatures as well as the highest temperature based on the comparison with experimental results, as depicted in Figure 10. It is also obvious that at the intermediate temperature range considerable deviation between prediction and experimental results is observed when only the thermal softening effects are considered, which is getting more pronounced with the increase of plastic deformation. These phenomena are consistent for all three loading directions in both materials, indicating the non-negligible contribution of the DSA to the flow stress of the investigated materials.

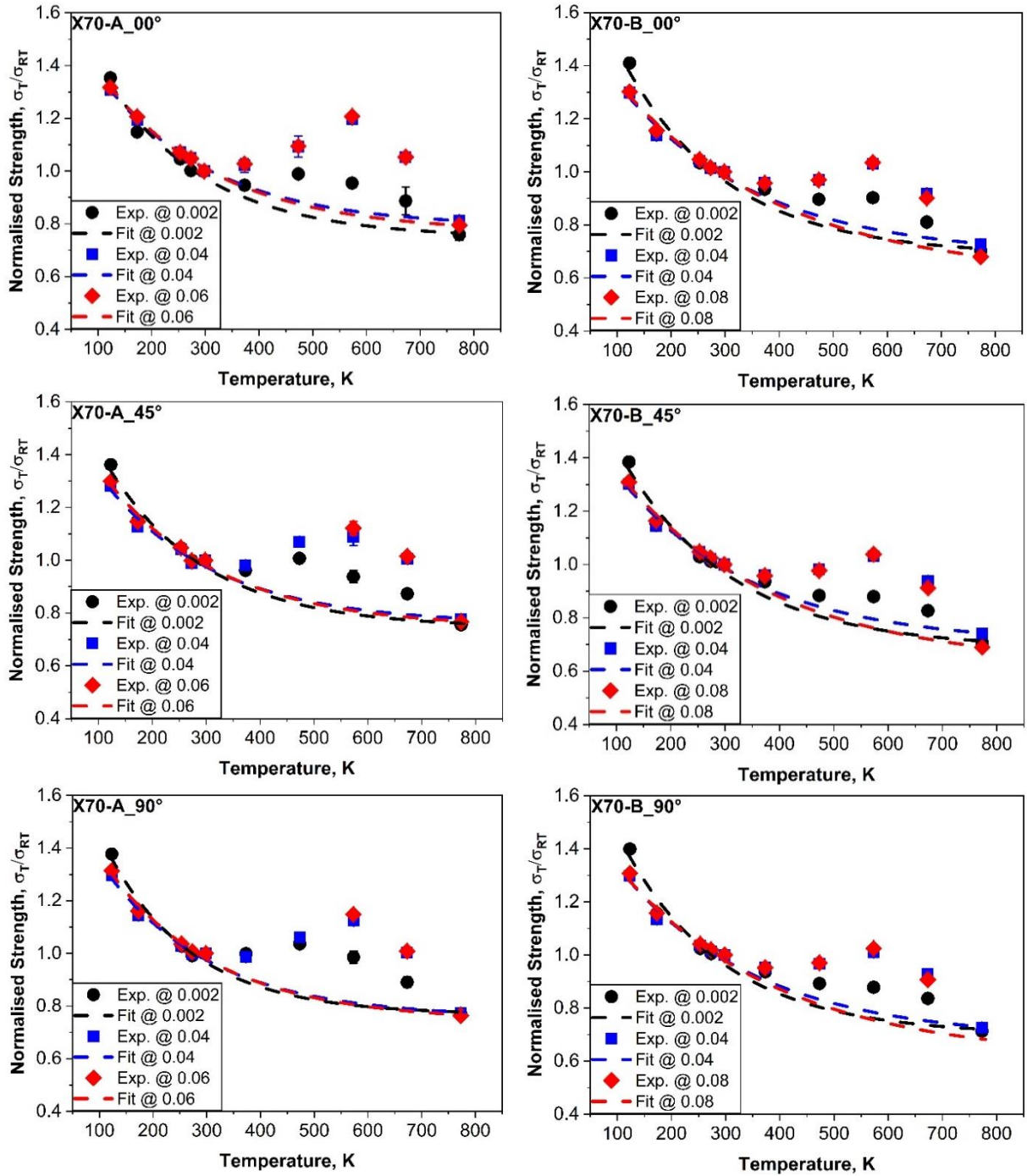


Figure 10: The prediction of the normalized strength considering only the thermal softening effects in comparison with experimental results at different plastic strain levels along three loading directions.

### 5.3 Dynamic strain aging component calibration

Based on the additive decomposition principle, the contribution from the DSA to the total thermal

effects on the flow stress is calculated by subtracting the thermal softening components from the experimental normalized strength. The parameters  $C_{4\sim6}$  in the DSA model can be easily calibrated using the resolved DSA components at corresponding temperatures and plastic strain levels for each loading direction in both materials. A comparison of the contribution of the DSA components between the fitting according to Eq. 12 and experimental results is demonstrated in Figure 11. A good consistency is achieved between the prediction and experimental results in the description of the bell-shaped distribution of the DSA intensity over temperature. It can be concluded that the DSA intensity is enhanced with the increase of plastic deformation, which is consistent with the theoretical expectation due to dislocation multiplication, as depicted in Figure 11. In addition, it is also observed that not only the peak intensity of the DSA component is enhanced by increasing plastic deformation, the peak position of the DSA intensity is also shifted to higher temperature values with the increase of plastic strain values, which is more obvious in X70-A. As mentioned in the model description section, the thermal parameter  $C_4$  and  $C_6$  describe the intensity of the DSA effects and the thermal parameter  $C_5$  corresponds to the characteristic temperature with the peak intensity of the DSA effects. Therefore, all the thermal parameters in the DSA models for three loading orientations in both materials should be evolving with the increase of plastic deformation. In addition, it is well known that the strain rate has a significant influence on the dynamic strain aging. In order to consider the effects of strain rate, a possible modification is necessary to make all thermal parameters depend also on the strain rate.

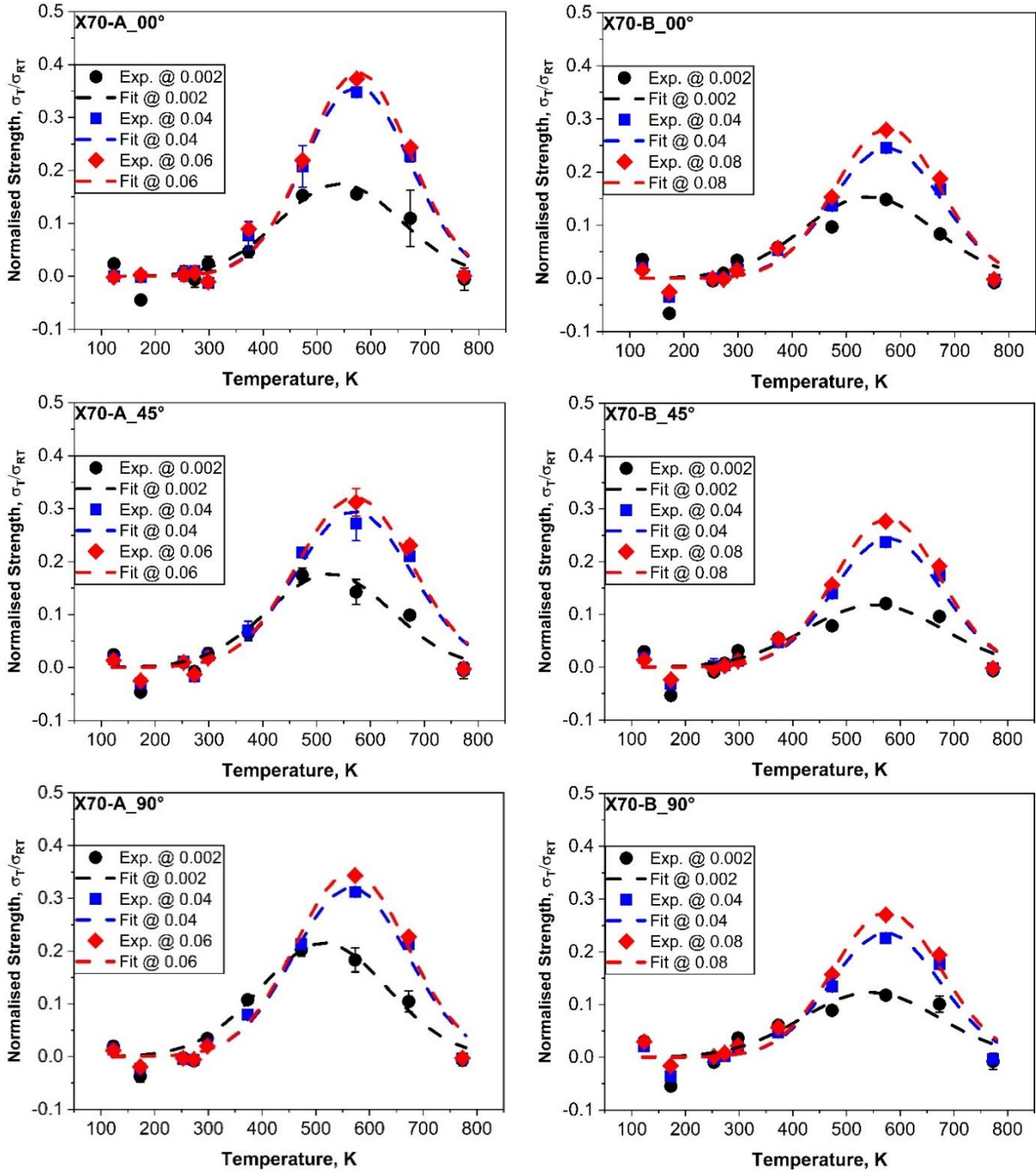


Figure 11: The prediction of the normalized strength contributed from the dynamic strain aging effects in comparison with experimental results at different plastic strain levels along three loading directions.

## 5.4 Combined thermal effects

With all the material parameters  $C_{1\sim6}$  in the thermal dependent model calibrated in the previous

sections, the overall thermal effects on flow stress are determined by adding the thermal softening component with the DSA component together according to Eq. 10-12. As shown in Figure 12, accurate prediction on the thermal effects is achieved in the complete temperature range at all strain levels and loading directions for both materials. As there are six parameters in the thermal dependent model, among which three are used for the characterization of thermal softening effects and the other three are devoted to describing the DSA effects, at least six valid experimental results over a wide range of temperature are required for the complete calibration of all parameters. When enough experimental results are not available, some assumptions can be made such as the thermal parameter  $C_5$  can be assigned as a constant, which is identical to the characteristic temperature value corresponding to the maximum DSA intensity. Another issue concerning the accuracy of the thermal dependent model is that the evolving features of plasticity shall be included as thermal effects on the flow stress show clear dependence on the degree of plastic deformation, as depicted in Figure 12. Therefore, the evolving features of thermal effects are further considered in the following.

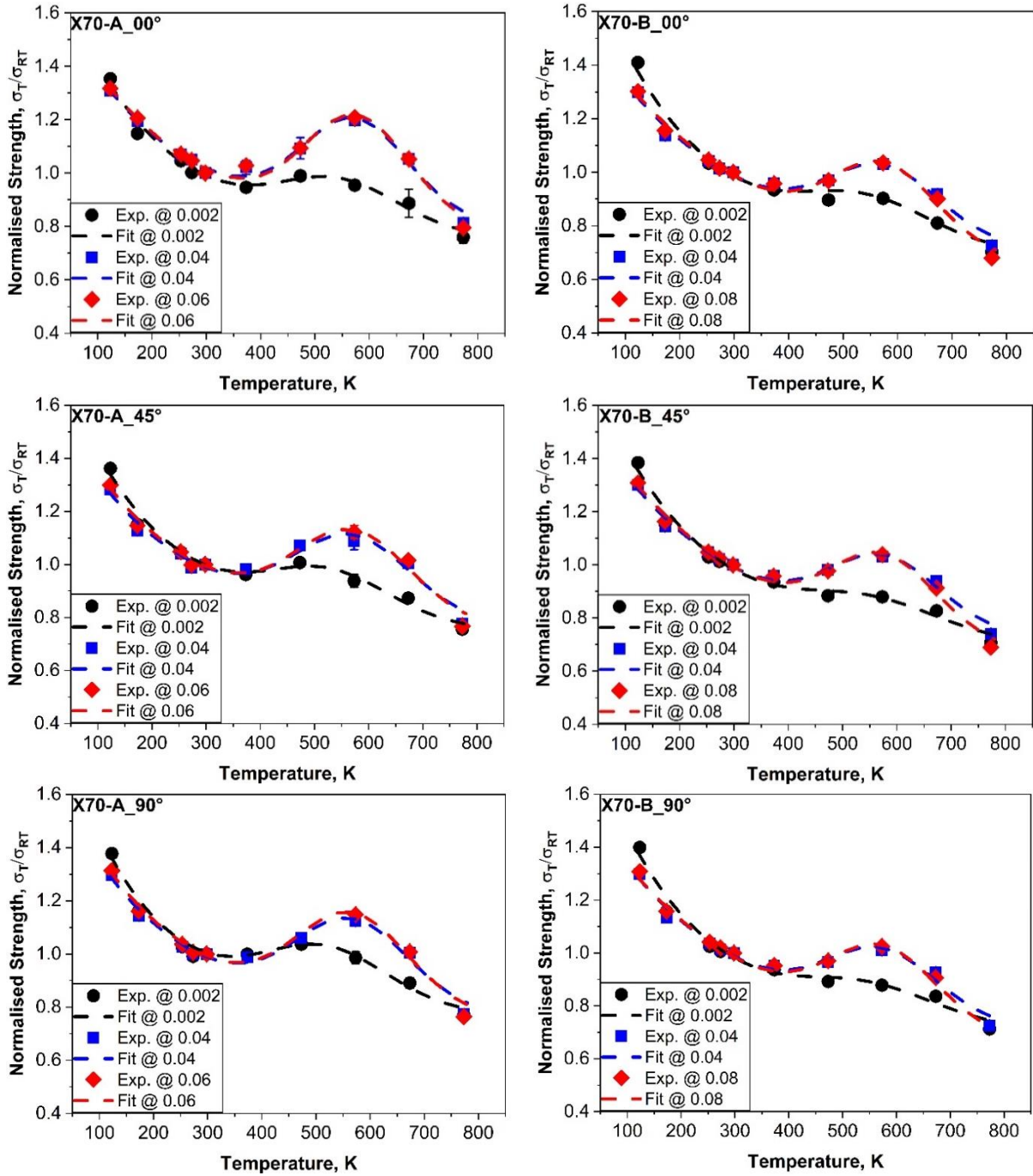


Figure 12: The prediction of the normalized strength considering thermal softening and dynamic strain aging effects in comparison with experimental results at different plastic strain levels along three loading directions.

## 5.5 Evolving features of material parameters

To capture the evolving features of plastic deformation, the thermal parameters  $C_{1\sim6}$  have been

calibrated at discrete true plastic strain values until the ultimate tensile strength point. The calibrated thermal parameters  $C_{1\sim 6}$  at different true plastic strain levels for individual loading directions are summarized in Table A 1 for X70-A and Table A 2 for X70-B in the Appendix. By applying the same method, the thermal parameters have been calibrated at three representative values of the PEEQ, which are listed in Table A 3 in the Appendix as well. A combination of exponential and third order polynomial functions according to Eq. 13 have been used to describe the evolving features of thermal parameters in this study. The corresponding parameters  $P_i^{0\sim 3}$  and  $Q_i^{1\sim 2}$  calibrated using the nonlinear least-squares algorithm for individual loading directions are summarized in Table A 4 for X70-A and Table A 5 for X70-B in the Appendix. The evolution of these thermal parameters is depicted in Figure 13 for X70-A and Figure 14 for X70-B, respectively. The solid symbols labeled ‘Fit’ represent the calibrated thermal parameters at discrete true plastic strain points according to Eq. 11-12. The dashed curves labeled ‘Evol.’ correspond to the continuous evolution functions of thermal parameters with strain according to Eq. 13.

Good fitting quality is achieved in describing the evolution of thermal parameters over a wide strain range in both steels. The evolution of individual parameter shares the same trend for three different loading directions in each material. For example, the thermal parameter  $C_5$  is increasing during the early stage of plastic deformation and approaching a plateau, indicating the characteristic temperature corresponding to the maximum DSA intensity is gradually shifting towards a constant value. In comparison with X70-A, it is obvious that the thermal parameters in X70-B show weaker dependence on the loading direction, meaning the thermal parameters are almost identical for three different orientations in material X70-B. This is consistent with the experimental observation that temperature has more pronounced impacts on anisotropy in X70-A than X70-B.

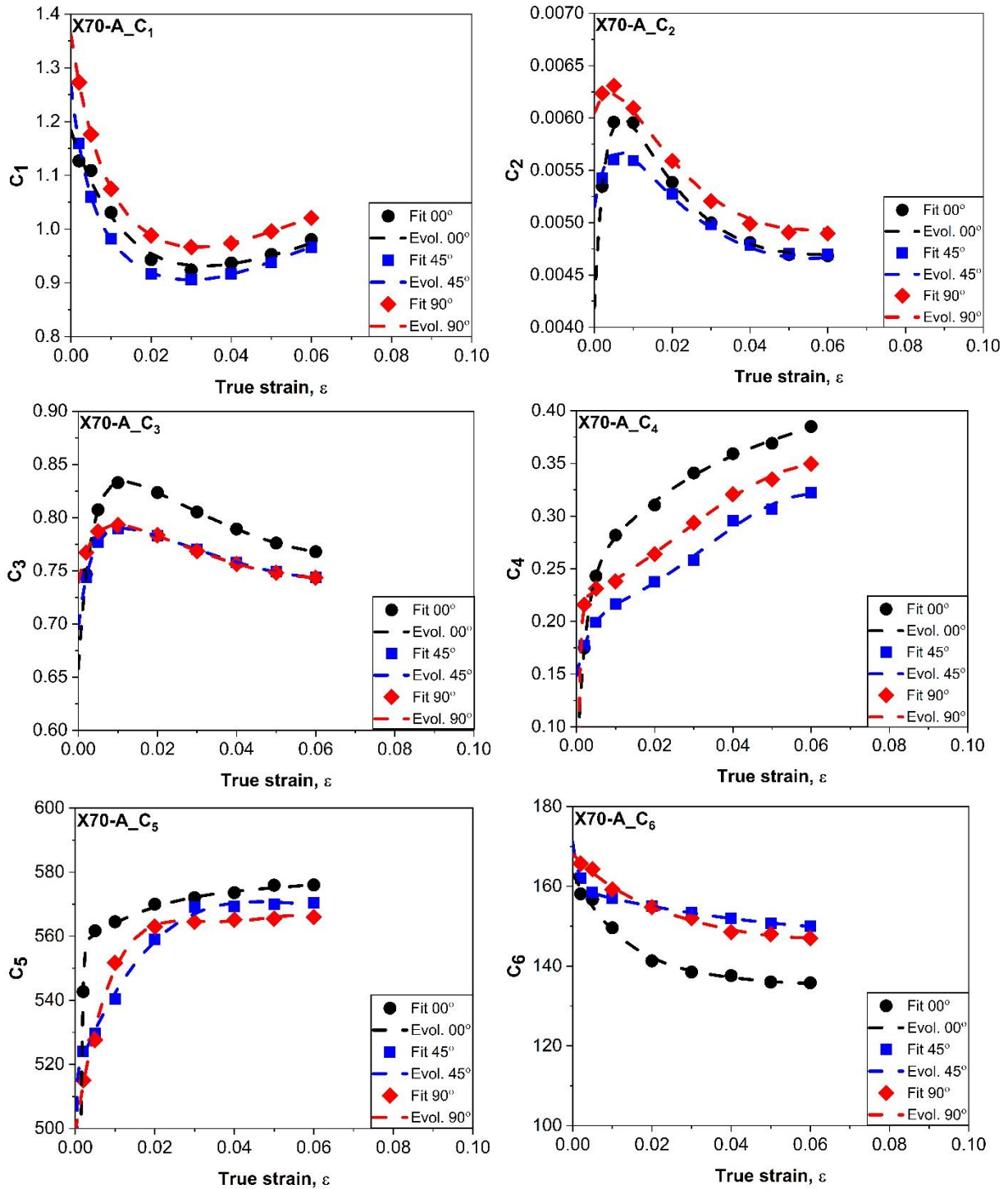


Figure 13: The evolution of the thermal parameters with true strain along three loading directions for X70-A.

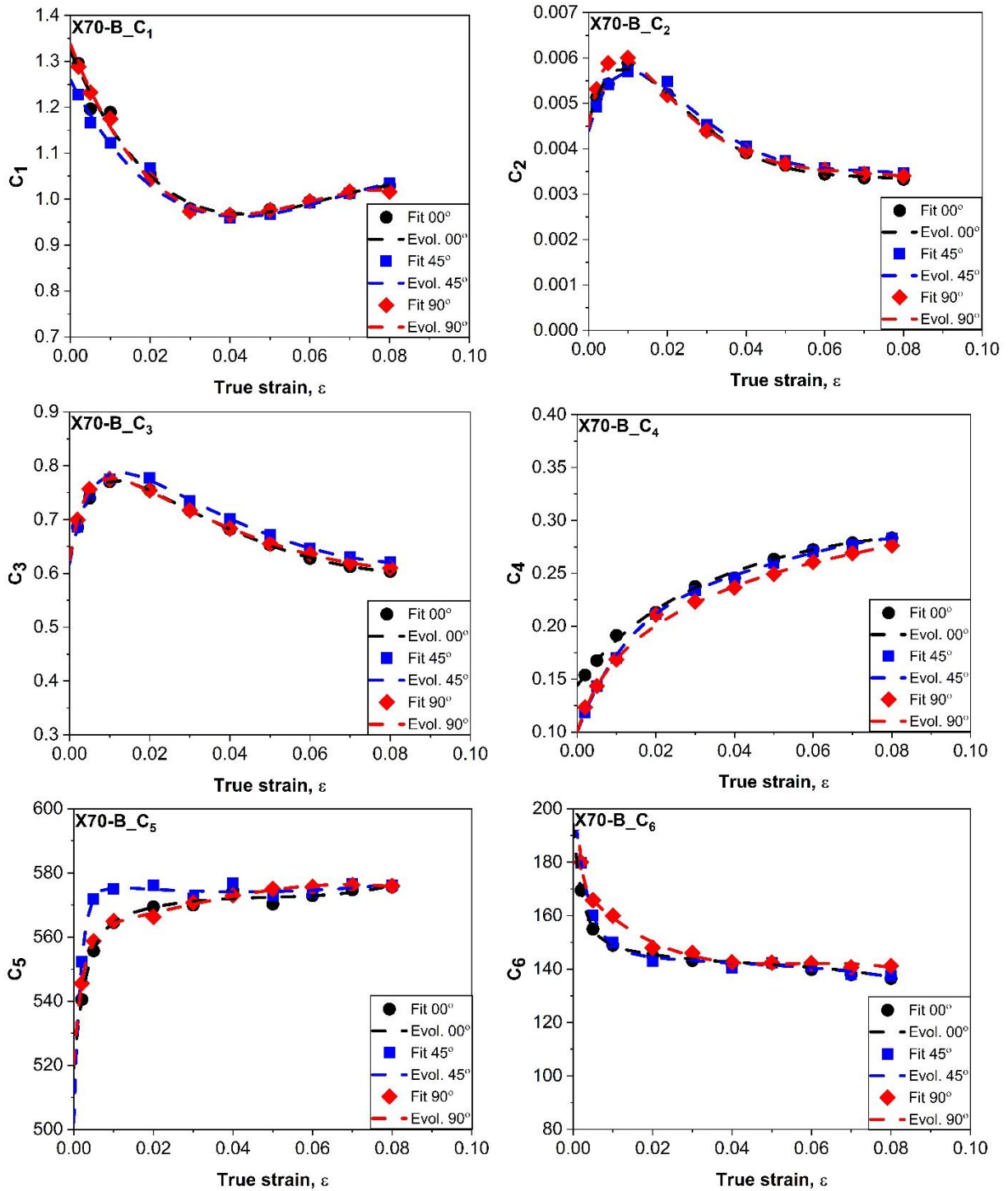


Figure 14: The evolution of the thermal parameters with true strain along three loading directions for X70-B.

Instead of calibrating thermal parameters at discrete plastic strain values, continuous flow curves for individual loading direction at different temperatures can be applied as an alternative approach in describing the evolution of thermal effects through using various extrapolation

models to describe the stress evolution with plastic strain. The latter approach is more important especially in the finite element simulation oriented applications, where further validation on the extrapolation law shall be provided. In this study, the focus is rather introducing the model and illustrating the methodology to employ the model, and therefore, the first approach is adopted.

## **5.6 Validation of the plasticity model**

Once the evolution of all thermal parameters is determined, the temperature effects quantified as  $f(T)$  can be described as continuous functions of plastic strain according to Eq. 16. Given the reference flow curve at RT along corresponding orientations, the complete description of flow curves within the valid true strain and temperature range can be predicted through multiplying the thermal effects. In order to achieve sufficiently precise prediction of the flow behavior over the complete temperature range, three individual experimental true stress–strain curves up to the maximum valid strain values at RT together with the thermal parameter evolution functions along  $0^\circ$ ,  $45^\circ$ , and  $90^\circ$  have been used. The predicted flow curves compared with experimental results at five representative temperatures along three loading directions are depicted in Figure 15, which verifies a good consistency within the temperature range from the minimum 123 K to the maximum 773 K for all three loading directions in both materials. The average stress values at 473 K are also accurately captured, where the most intensive jerky flow behavior is observed, validating the efficiency and accuracy of the plasticity model in the description of evolutionary thermal effects on the plastic flow behavior even with the existence of the DSA. Depending on the specific temperatures, the flow curves show distinct characteristics. At certain temperatures, a Lüders band exists and its length, i.e. the value of Lüders strain varies with temperature and loading orientation. The strain hardening behavior is also changing with temperature, such as the flow curve at 773 K is approaching a saturation type while that of 123 K possesses a more constant hardening rate. In general, excellent accuracy in describing the flow curves with

different shapes and characteristics is achieved using the analytical plasticity model, which is not provided by other analytical models so far (Wang et al., 2015). The level of precision of the delivered results using the current analytical model is comparable to that of the machine-learning model reported by Li et al. (2019), which relies on a large dataset for model training. The analytical material models provide the advantages of the straightforward implementation into finite element based platforms for potential applications such as in the field of material forming.

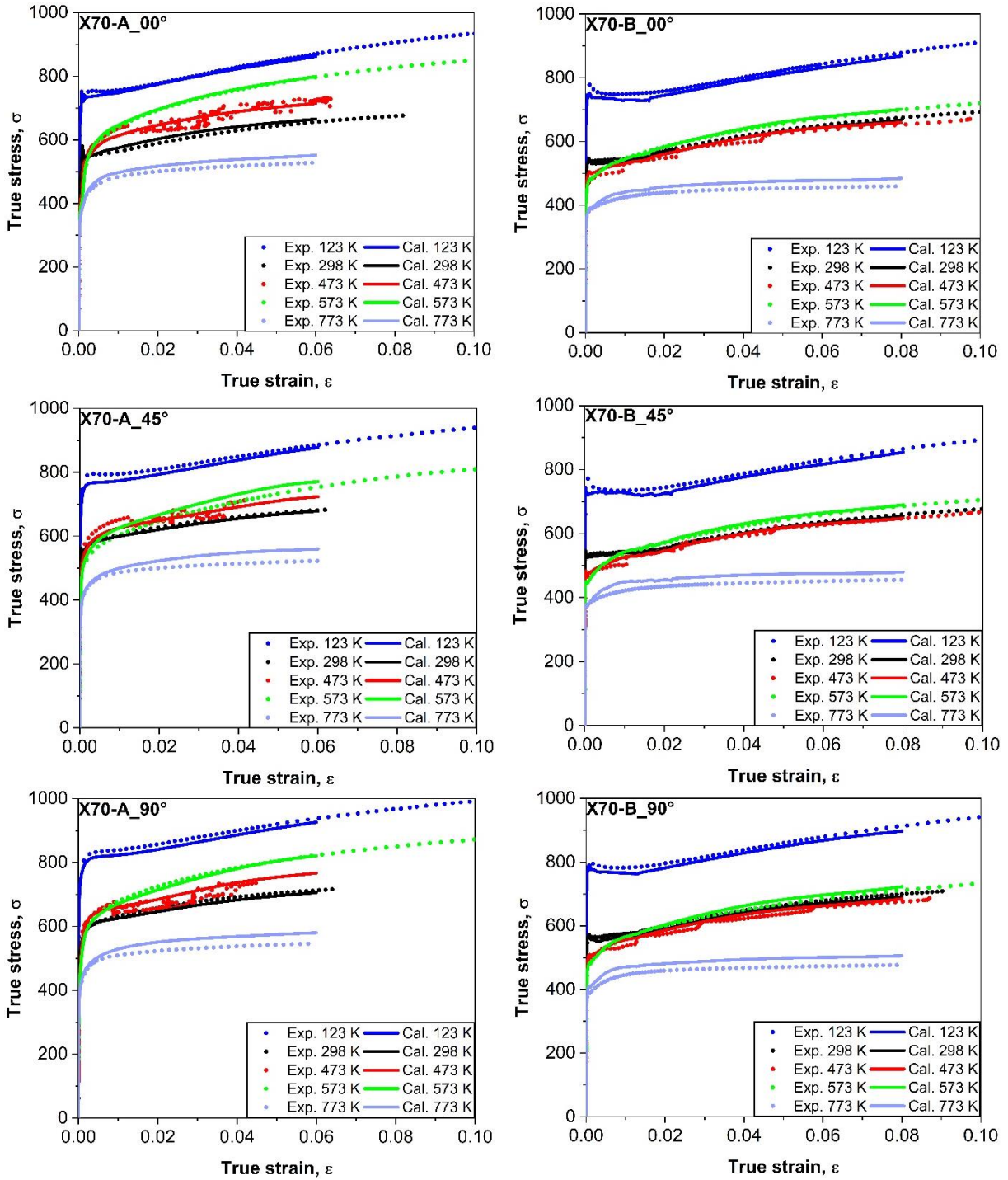


Figure 15: The prediction of flow curves in comparison with experimental results along three loading directions at five representative temperatures.

## 6 Discussion

### 6.1 The thermal-dependent flow stress

The normalized strength as a quantification variable of the thermal effects has a clear dependence on temperature and strain, as depicted in Figure 16. The non-monotonic change of the normalized strength is exhibited with the increase of temperature and the peak value is observed at intermediate temperatures, which correspond to the intensive region of the DSA. The continuous surface plotted in the space of temperature, strain and normalized strength is calculated based on the evolution of thermal parameters for each individual loading direction. It is obvious that the experimental data are located on the predicted surface, verifying the high accuracy of the constitutive model in the description of thermal effects for the investigated materials. It is also easy to conclude from the results in Figure 16 that significant errors will occur if the evolution of thermal parameters is not properly considered.

When digging into details, it is found that the thermal impacts on the flow behavior depend on both the specific material and the loading direction. In general, the intensity of the DSA is more pronounced in X70-A than X70-B, which might be resulting from the difference in the microstructure of these two materials. The shape of the three-dimensional surface of the normalized strength is almost identical for three loading directions in X70-B, indicating the thermal effects show very weak anisotropic behavior in this material. In contrast, quite distinguished thermal effects are noticed along three loading directions in X70-A and the intensity of the DSA is the most pronounced along the  $0^\circ$  direction. Therefore, the interaction between anisotropy and thermal impacts on the flow behavior should be further analyzed and revealed in more detail. It is common in both materials, the evolution of thermal parameters plays important roles in the accurate description of the thermal influence on the flow behavior.

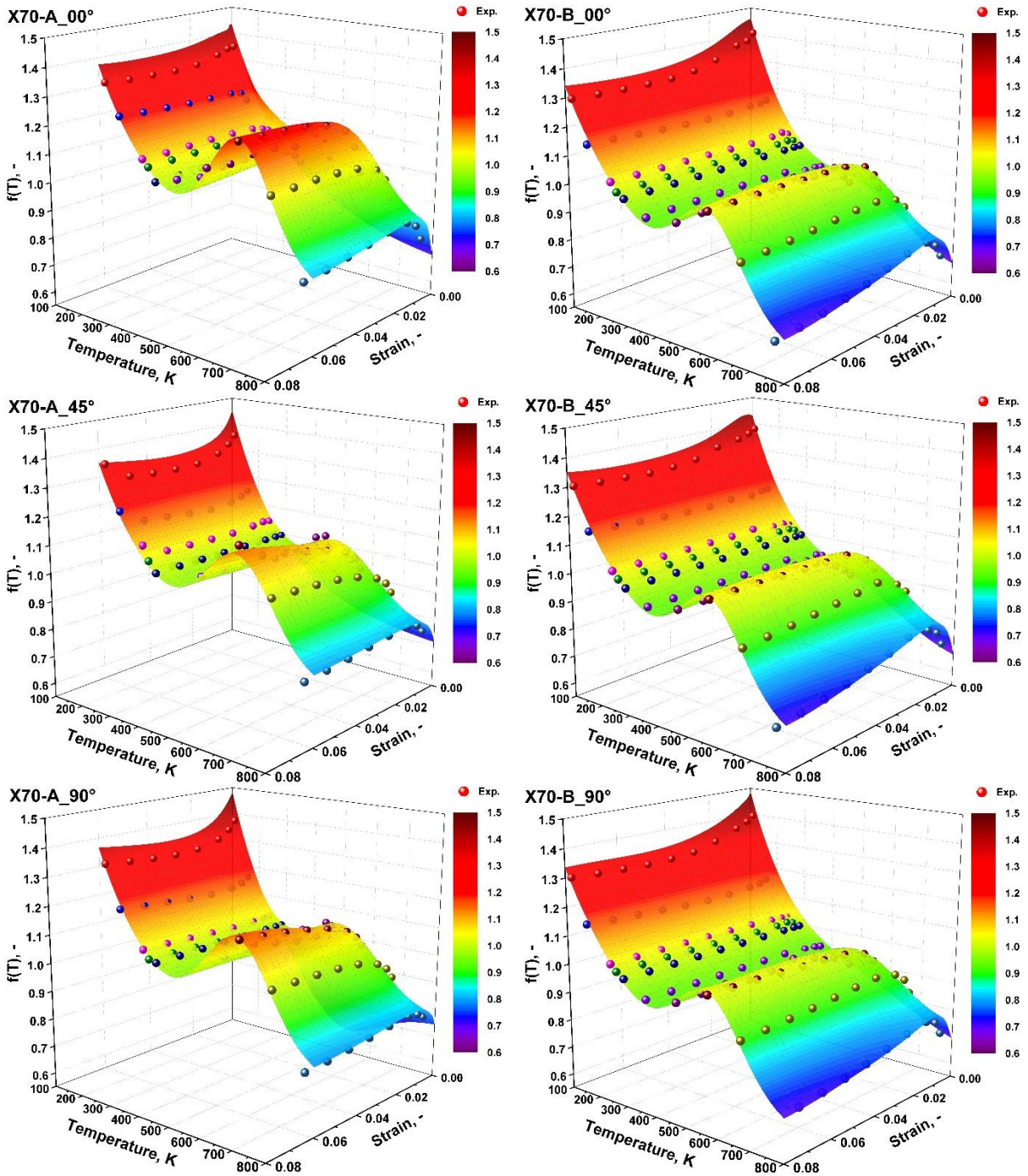


Figure 16: The prediction of the distribution of the normalized strength over the strain and temperature in comparison with experimental results from uniaxial tensile tests along three loading directions.

When the distribution of the normalized strength over the entire strain and temperature range is determined, the corresponding true stress at certain true strain values at any temperatures can be

calculated by multiplying with the true stress at the reference temperature, as depicted in Figure 17. The constructed surface in the space of true stress, true plastic strain and temperature agrees well with all experimental results within the valid range of temperature and strain, proving that the evolving plasticity model developed in this study can accurately, efficiently and completely represent the flow behavior of the investigated materials over a broad range of temperature. Instead of treating the material along each loading direction as an independent constituent, the material with distinguished properties along different directions is treated as an entity by incorporating the anisotropic plasticity model. Therefore, the flow behavior along any loading direction (besides the  $0^\circ$ ,  $45^\circ$  and  $90^\circ$  used for parameter calibration) at any temperatures can be predicted using this evolving plasticity model. The response of the material is affected by many variables, such as deformation degree and loading rates. For example, DSA is suppressed by high loading rates. Therefore, the constitutive model needs further validations in other loading scenarios, such as at higher deformation levels and/or under different strain rates. However, it is not the major aim of this study to perform a comprehensive calibration of all model parameters and accurately describe material properties under different loading conditions. The major highlight of this study is to propose a new approach or methodology in capturing the thermal impacts on the flow behavior of metallic materials even with the existence of sophisticated deformation mechanisms, such as DSA that is frequently observed in many materials. In addition, an emphasis has been focused on the evolving features of plastic deformation as well as the influence of temperature on anisotropy, which shall not be overlooked for the precise description of flow behavior. In order to identify the material parameters in the developed constitutive plasticity model, no additional experimental efforts are required and only a straightforward and more precise evaluation approach is necessary to achieve higher accuracy, especially when the microstructural evolution, as well as the DSA, is very pronounced.

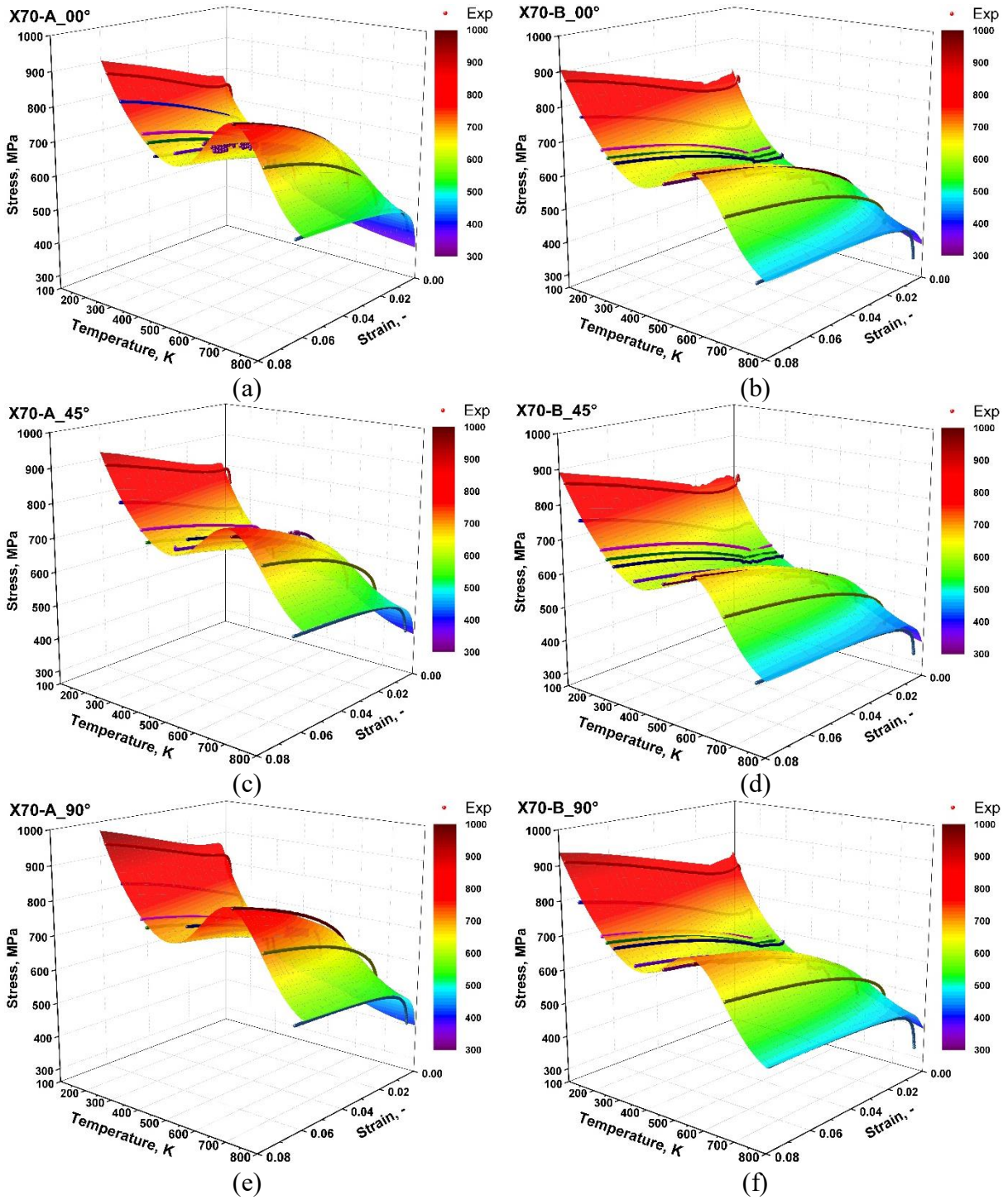


Figure 17: The prediction of the flow curves at different temperatures in comparison with experimental results from uniaxial tensile tests along three loading directions.

## 6.2 Coupling anisotropy with thermal effects

In order to completely and directly visualize the thermal effects on anisotropic plasticity, the

evolution of the yield locus with the temperature at three different values of the PEEQ is depicted in Figure 18 for both materials. For the construction of such a surface, the normalized strength along  $0^\circ$ ,  $45^\circ$  and  $90^\circ$  at different temperatures are used as input data, which are calculated based on the thermal parameters  $C_{1\sim6}$  for individual loading directions as well as the flow stress at RT at the corresponding values of the PEEQ. For the reason of easy visualization, the results at only three PEEQ values are shown. However, when the evolution of thermal parameters as functions of the PEEQ are determined, the complete overview of the yield locus at any specific values of PEEQ can be predicted. The solid points in the figure represent the experimental results of uniaxial tension along  $0^\circ$  and  $90^\circ$  as well as the biaxial tension state. The stress states corresponding to the uniaxial tensile along  $0^\circ$  and  $90^\circ$ , as well as the equibiaxial tension, are represented by solid lines with different colors on the yield locus at different temperatures. The variation of the yield locus with temperature is not obvious in X70-B as there is almost no change in the yield locus at different temperatures and the characteristic stress states lie on a straight line. For instance, the uniaxial tensile state along  $0^\circ$  and the equibiaxial tension are represented by two straight lines parallel to the temperature axis. In contrast, the yield locus is affected by temperature to a larger extent in X70-A as the yield locus fluctuates intensively with the increase of temperature. The points corresponding to the characteristic stress states of uniaxial or equibiaxial tension are not on a straight line parallel to the temperature axis but fluctuating with temperature in X70-A. These phenomena are consistent with the observation that temperature has more pronounced impacts on the anisotropy in X70-A than X70-B.

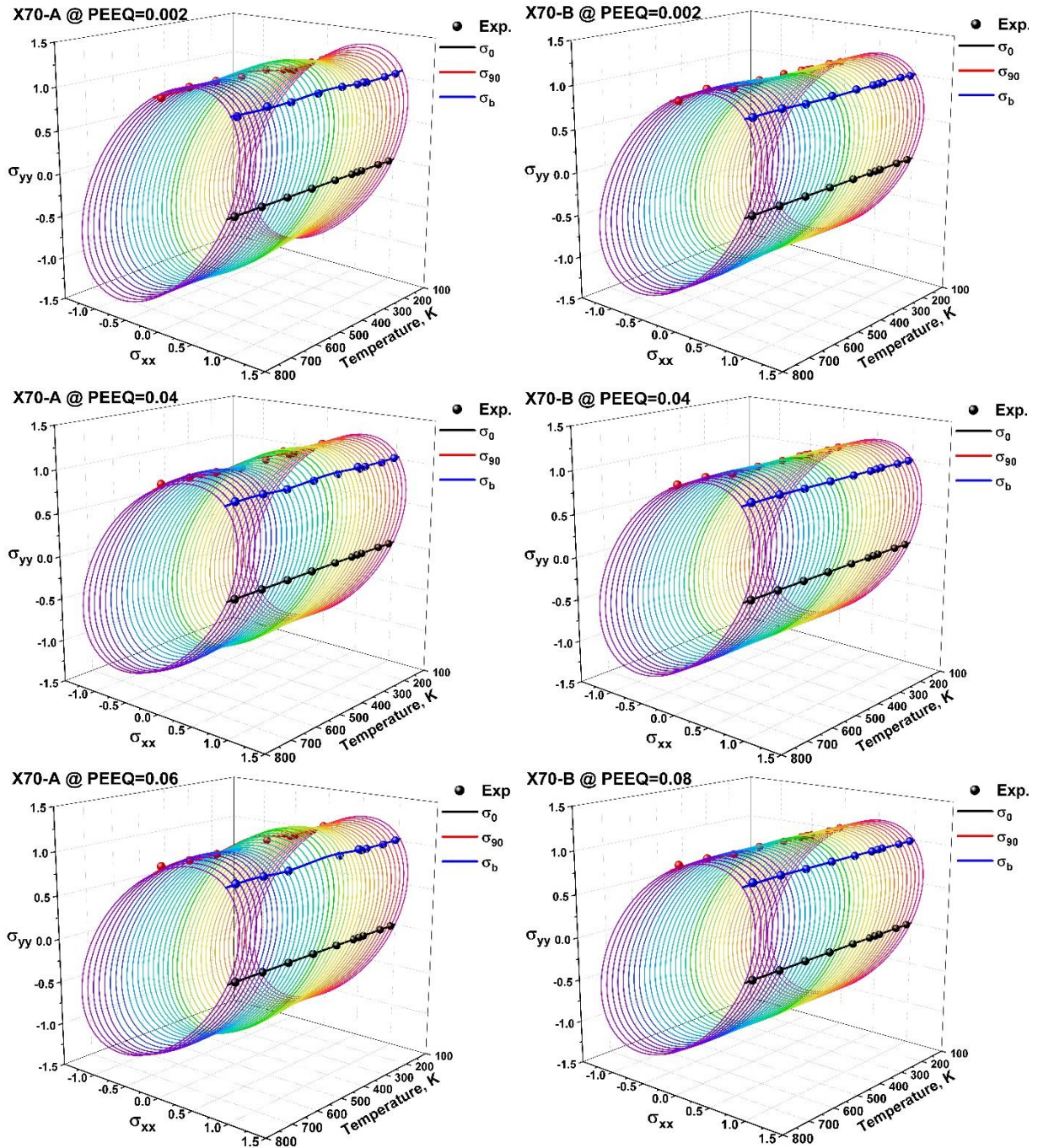


Figure 18: The evolution of the yield locus with temperature determined from tensile tests at three representative equivalent plastic strain levels.

An alternative approach to evaluating the thermal effects on anisotropy in a more direct way is to construct a surface of the distribution of the normalized stress over the loading direction and temperature, as depicted in Figure 19. The experimental results of the normalized stress along  $0^\circ$ ,  $45^\circ$  and  $90^\circ$  are represented by solid points with different colors. It is obvious that the distribution

of the normalized stress over the loading direction shows weaker dependence on temperature in X70-B in comparison with X70-A, especially at relatively larger equivalent plastic strain levels of 0.04 and 0.08. For example, the surface of the normalized stress at the PEEQ of 0.04 in X70-B is extending almost parallel along the temperature axis. The cross-section of the surface at different temperatures is almost identical, indicating the weak dependence of anisotropy on the temperature in X70-B. In contrast, the surface of the normalized stress at all three different PEEQ values in X70-A is fluctuating significantly along the temperature axis. The cross-section of the surface at different temperatures is obviously not coincident with each other in X70-A. In addition to the pronounced effects of temperature on the normalized stress distribution, the influence of plastic strain on the normalized stress distribution is also very significant in X70-A. Obviously, the distribution of the normalized stress is changing with the increase of plastic deformation in this material. For example, the stress distribution at the yield point shows that the rolling direction has the lowest yield strength, however, with the increase of plastic deformation the minimum stress shifts to the diagonal direction in X70-A at some temperatures. The thermal effects and the influence of plastic strain on the normalized stress are not independent of each other because at different strain levels the impacts of temperature are also varied. These observations indicate the significant importance of the evolving thermal effects on the flow behavior of metallic materials, which can be accurately predicted by the evolving plasticity model proposed in this study even when the complicated DSA deformation mechanism is activated.

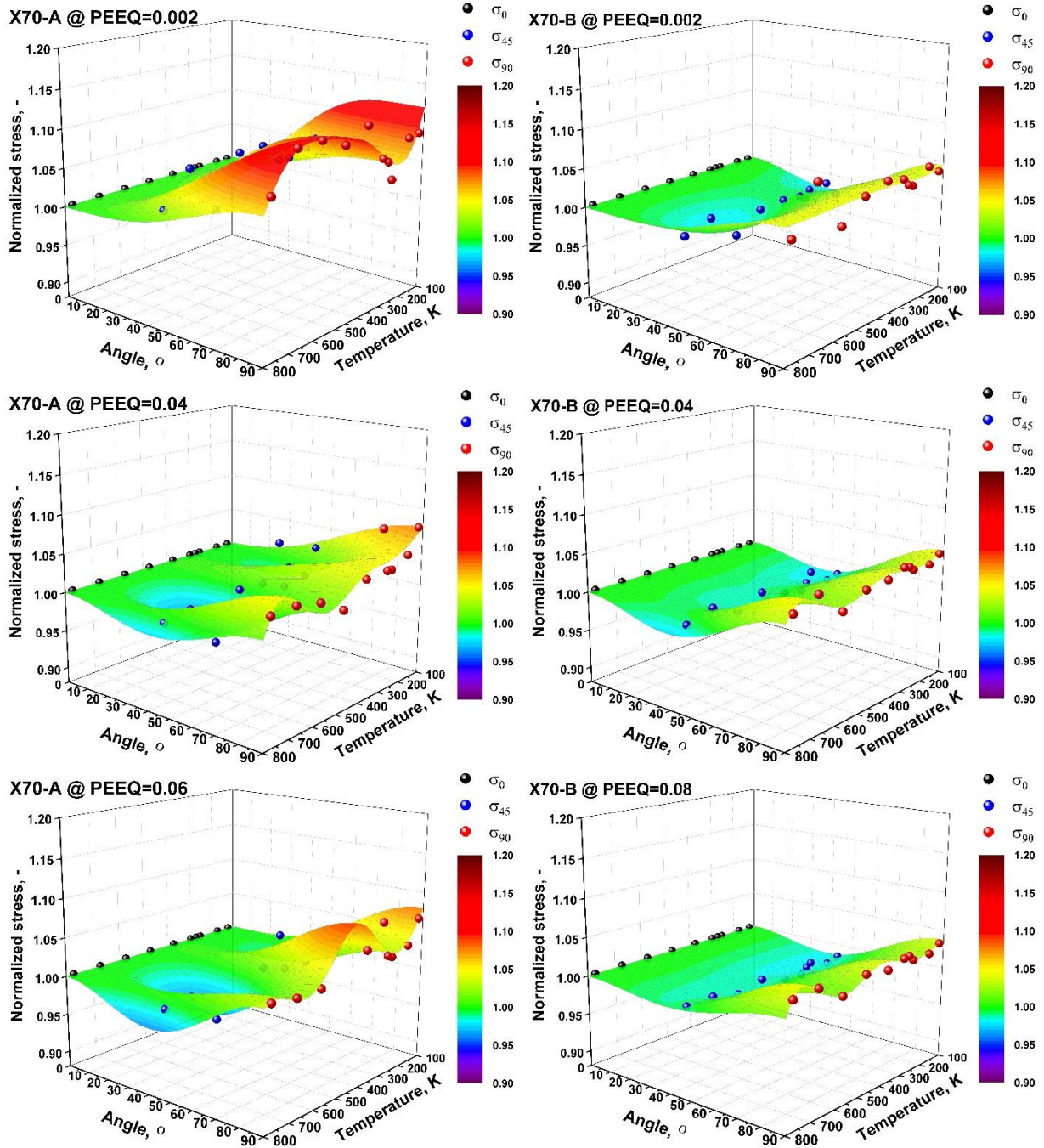


Figure 19: The distribution of the normalized stress over the loading angle and temperature determined from uniaxial tensile tests at three representative equivalent plastic strain levels.

## 7 Conclusions

The thermal effects on the anisotropic flow behavior of two high–strength steels have been comprehensively characterized through performing quasi-static uniaxial tensile tests following different orientations over a broad range of temperatures. An evolving plasticity model has been proposed to describe the complicated thermal affected anisotropic plastic flow of the investigated materials. Based on the results presented in this study, several conclusions can be drawn.

- The temperature has a non-monotonic influence on the flow behavior of the investigated high–strength steels due to the occurrence of the dynamic strain aging.
- The evolution of thermal parameters plays significant roles in the description of thermal affected plastic flow behavior, especially when complicated deformation mechanisms such as the dynamic strain aging are activated.
- The influence of temperature on the anisotropy of metallic materials depends on the investigated material. For the same grade of steels in this study, pronounced thermal impacts on the anisotropy are only observed in one material, while a negligible thermal sensitivity is found for the other one.
- A generalized evolving plasticity model considering the evolutionary features of strain hardening and thermal effects provides high accuracy in capturing the anisotropic plastic flow behavior of high–strength steels over a wide range of temperatures.

## **Acknowledgment**

The authors are thankful for thyssenkrupp Steel Europe AG for the materials supply as well as financial support.

## Appendix: Calibrated thermal parameters at different strain levels

Table A 1: Calibrated thermal parameters at different plastic strain levels along three loading directions for X70-A

Constants	0.002	0.005	0.01	0.02	0.03	0.04	0.05	0.06	
$\theta = 0^\circ$	$C_1$	1.127	1.109	1.031	0.943	0.924	0.937	0.953	0.981
	$C_2$	0.00535	0.00596	0.00596	0.00539	0.00500	0.00481	0.00469	0.00468
	$C_3$	0.747	0.807	0.833	0.824	0.805	0.789	0.776	0.768
	$C_4$	0.175	0.243	0.282	0.310	0.341	0.359	0.369	0.385
	$C_5$	543	562	565	570	572	574	576	576
	$C_6$	158	157	150	141	139	138	136	136
$\theta = 45^\circ$	$C_1$	1.159	1.060	0.982	0.917	0.906	0.916	0.938	0.967
	$C_2$	0.00543	0.00560	0.00559	0.00528	0.00498	0.00479	0.00471	0.00470
	$C_3$	0.744	0.777	0.789	0.783	0.770	0.758	0.749	0.744
	$C_4$	0.177	0.199	0.217	0.237	0.258	0.296	0.307	0.322
	$C_5$	524	530	540	559	569	569	570	570
	$C_6$	162	159	157	155	153	152	151	150
$\theta = 90^\circ$	$C_1$	1.273	1.176	1.075	0.988	0.967	0.974	0.996	1.021
	$C_2$	0.00623	0.00631	0.00610	0.00559	0.00520	0.00499	0.00491	0.00490
	$C_3$	0.767	0.787	0.793	0.783	0.769	0.756	0.748	0.744
	$C_4$	0.216	0.231	0.238	0.264	0.294	0.321	0.335	0.350
	$C_5$	515	528	552	563	565	565	566	566
	$C_6$	166	164	159	155	152	149	148	147

Table A 2: Calibrated thermal parameters at different plastic strain levels along three loading directions for X70-B

Constants	0.002	0.005	0.01	0.02	0.03	0.04	0.05	0.06	0.07	0.08	
$\theta = 0^\circ$	$C_1$	1.295	1.196	1.189	1.054	0.979	0.965	0.978	0.995	1.013	1.029
	$C_2$	0.00513	0.00543	0.00589	0.00520	0.00439	0.00391	0.00363	0.00344	0.00336	0.00333
	$C_3$	0.686	0.740	0.770	0.755	0.717	0.682	0.653	0.628	0.613	0.604
	$C_4$	0.154	0.168	0.191	0.213	0.238	0.246	0.263	0.273	0.279	0.283
	$C_5$	541	556	565	569	570	574	570	573	575	576
	$C_6$	170	155	149	145	143	142	142	140	138	137
$\theta = 45^\circ$	$C_1$	1.227	1.166	1.122	1.068	0.977	0.959	0.968	0.992	1.012	1.034
	$C_2$	0.00493	0.00542	0.00570	0.00549	0.00453	0.00406	0.00374	0.00357	0.00349	0.00347
	$C_3$	0.686	0.746	0.775	0.777	0.734	0.702	0.671	0.646	0.631	0.620
	$C_4$	0.118	0.143	0.170	0.212	0.234	0.245	0.260	0.271	0.277	0.283
	$C_5$	552	572	575	576	572	577	573	574	577	576
	$C_6$	180	160	150	143	145	140	142	141	138	137
$\theta = 90^\circ$	$C_1$	1.288	1.232	1.175	1.043	0.973	0.966	0.976	0.995	1.016	1.016
	$C_2$	0.00532	0.00589	0.00601	0.00519	0.00440	0.00395	0.00367	0.00354	0.00345	0.00340
	$C_3$	0.699	0.756	0.775	0.754	0.717	0.683	0.656	0.636	0.620	0.610
	$C_4$	0.123	0.144	0.169	0.211	0.223	0.237	0.249	0.261	0.269	0.276
	$C_5$	546	559	565	566	571	573	575	576	576	576
	$C_6$	180	166	160	148	146	143	142	142	141	141

Table A 3: Calibrated thermal parameters at three different values of the equivalent plastic strain (PEEQ) along three loading directions for X70-A and X70-B

Constants		X70-A			X70-B		
PEEQ		0.002	0.04	0.06	0.002	0.04	0.08
$\theta = 0^\circ$	$C_1$	1.127	0.937	0.981	1.295	0.965	1.029
	$C_2$	0.00535	0.00481	0.00468	0.00513	0.00391	0.00333
	$C_3$	0.747	0.789	0.768	0.686	0.682	0.604
	$C_4$	0.175	0.359	0.385	0.154	0.246	0.283
	$C_5$	543	574	576	541	574	576
	$C_6$	158	138	136	170	142	137
$\theta = 45^\circ$	$C_1$	1.401	1.008	1.054	1.267	0.987	1.080
	$C_2$	0.00697	0.00398	0.00424	0.00503	0.00341	0.00293
	$C_3$	0.778	0.652	0.661	0.684	0.632	0.540
	$C_4$	0.194	0.360	0.377	0.139	0.273	0.310
	$C_5$	493	571	572	556	579	580
	$C_6$	165	178	179	175	147	143
$\theta = 90^\circ$	$C_1$	1.480	1.076	1.150	1.309	0.983	1.068
	$C_2$	0.00726	0.00405	0.00412	0.00504	0.00364	0.00307
	$C_3$	0.773	0.633	0.611	0.670	0.644	0.553
	$C_4$	0.243	0.389	0.448	0.156	0.251	0.294
	$C_5$	515	577	566	565	578	577
	$C_6$	168	178	180	173	146	145

Table A 4: Calibrated material parameters describing the evolution of thermal parameters over plastic strain along three loading directions for X70-A

Constants	$C_1$	$C_2$	$C_3$	$C_4$	$C_5$	$C_6$	
$\theta = 0^\circ$	$P^0$	0.3093	0.006905	0.8606	0.2412	556.6	-221.7
	$P^1$	19.05	-0.1067	-1.69	4.59	896.5	8867
	$P^2$	-207.1	1.725	-12.09	-52.68	-15600	-90710
	$P^3$	1003	-9.346	242	263.9	101400	371200
	$Q^1$	0.8742	-0.002719	-0.2024	-0.1871	-2801	384.8
	$Q^2$	47.39	341.1	303	454	2679	28
$\theta = 45^\circ$	$P^0$	1.054	0.006254	0.8041	0.2203	516.4	159.1
	$P^1$	-11.47	-0.0648	-0.7222	-0.9738	3144	-229.7
	$P^2$	267.6	0.7821	-22.78	113.9	-59540	1216
	$P^3$	-1679	-2.387	301.4	-1162	367200	1153
	$Q^1$	0.2133	-0.001107	-0.108	-0.0722	-259700	12.01
	$Q^2$	259.3	268.8	304.7	270.7	22380	643.6
$\theta = 90^\circ$	$P^0$	1.101	0.006891	0.8127	0.2217	1190	131.9
	$P^1$	-10.51	-0.08602	-1.379	1.348	-24150	701.4
	$P^2$	243.5	1.188	-9.362	54.45	356000	-13880
	$P^3$	-1509	-4.936	219	-694.8	-1922000	97720
	$Q^1$	0.2612	-0.0008423	-0.07355	-0.3838	-691.3	36.17
	$Q^2$	152.4	232	270.9	1876	46.9	48.86

Table A 5: Calibrated material parameters describing the evolution of thermal parameters over plastic strain along three loading directions for X70-B

Constants	$C_1$	$C_2$	$C_3$	$C_4$	$C_5$	$C_6$	
$\theta = 0^\circ$	$P^0$	-0.311	0.009127	0.8591	0.248	560.8	151.9
	$P^1$	-3.51	-0.2376	-5.456	0.135	641.2	-456.6
	$P^2$	267.5	3.334	23.3	11.78	-12430	7836
	$P^3$	-1612	-15.87	62.18	-95.25	84970	-55800
	$Q^1$	1.633	-0.004529	-0.2357	-0.1042	-41.69	42.25
	$Q^2$	9.979	124.3	186.6	49.21	331.3	412.1
$\theta = 45^\circ$	$P^0$	-0.7209	0.01016	0.875	0.408	576.7	148.1
	$P^1$	-6.087	-0.2754	-5.124	-5.976	-116.1	-265.1
	$P^2$	261.1	3.862	15.24	92.12	1167	4400
	$P^3$	-1408	-18.32	112.8	-451.6	3094	-35130
	$Q^1$	1.98	-0.005764	-0.2572	-0.3081	-74.5	56.91
	$Q^2$	5.339	101.8	182.2	51.46	564.8	285.9
$\theta = 90^\circ$	$P^0$	-4.168	0.008204	0.842	0.1453	562.2	173.1
	$P^1$	16.7	-0.1997	-4.798	3.467	242	-1670
	$P^2$	275.2	2.895	18.63	-35.1	1951	29480
	$P^3$	-2050	-14.39	64.23	153.1	-35780	-171000
	$Q^1$	5.505	-0.003723	-0.2171	-0.04486	-41.84	90.6
	$Q^2$	7.02	200.1	246.1	176.5	444.2	1094

## References

- Abedrabbo, N., Pourboghrat, F., Carsley, J., 2006a. Forming of aluminum alloys at elevated temperatures – Part 1: Material characterization. *International Journal of Plasticity* 22, 314-341.
- Abedrabbo, N., Pourboghrat, F., Carsley, J., 2006b. Forming of aluminum alloys at elevated temperatures – Part 2: Numerical modeling and experimental verification. *International Journal of Plasticity* 22, 342-373.
- Aboufadel, H., Deges, J., Choi, P., Raabe, D., 2015. Dynamic strain aging studied at the atomic scale. *Acta Materialia* 86, 34-42.
- Aretz, H., Barlat, F., 2013. New convex yield functions for orthotropic metal plasticity. *International Journal of Non-Linear Mechanics* 51, 97-111.
- Bai, Y., Wierzbicki, T., 2008. A new model of metal plasticity and fracture with pressure and Lode dependence. *International Journal of Plasticity* 24, 1071-1096.
- Banabic, D., Aretz, H., Comsa, D.S., Paraianu, L., 2005. An improved analytical description of orthotropy in metallic sheets. *Int. J. Plasticity* 21, 493-512.
- Banabic, D., Barlat, F., Cazacu, O., Kuwabara, T., 2010. Advances in anisotropy and formability. *International Journal of Material Forming* 3, 165-189.
- Bandyopadhyay, K., Basak, S., Prasad, K.S., Lee, M.-G., Panda, S.K., Lee, J., 2019. Improved formability prediction by modeling evolution of anisotropy of steel sheets. *International Journal of Solids and Structures* 156-157, 263-280.
- Barlat, F., Aretz, H., Yoon, J.W., Karabin, M.E., Brem, J.C., Dick, R.E., 2005a. Linear transformation-based anisotropic yield functions. *International Journal of Plasticity* 21, 1009-1039.
- Barlat, F., Brem, J.C., Yoon, J.W., Chung, K., Dick, R.E., Lege, D.J., Pourboghrat, F., Choi, S.H., Chu, E., 2003. Plane stress yield function for aluminum alloy sheets—part I: theory. *Int. J. Plasticity* 19, 1297-1319.
- Barlat, F., Cazacu, O., Źyczkowski, M., Banabic, D., Yoon, J.W., 2005b. Yield Surface Plasticity and Anisotropy. *Continuum Scale Simulation of Engineering Materials*.
- Barlat, F., Gracio, J.J., Lee, M.-G., Rauch, E.F., Vincze, G., 2011. An alternative to kinematic hardening in classical plasticity. *International Journal of Plasticity* 27, 1309-1327.
- Barlat, F., Lege, D.J., Brem, J.C., 1991. A six-component yield function for anisotropic materials. *International Journal of Plasticity* 7, 693-712.
- Barlat, F., Lian, J., 1989. Plastic Behavior and Stretchability of Sheet Metals .1. A Yield Function

for Orthotropic Sheets under Plane-Stress Conditions. *Int. J. Plasticity* 5, 51-66.

Benallal, A., Berstad, T., Børvik, T., Hopperstad, O.S., Koutiri, I., de Codes, R.N., 2008. An experimental and numerical investigation of the behaviour of AA5083 aluminium alloy in presence of the Portevin–Le Chatelier effect. *International Journal of Plasticity* 24, 1916-1945.

Bodner, S.R., Partom, Y., 1975. Constitutive Equations for Elastic-Viscoplastic Strain-Hardening Materials. *J. Appl. Mech.* 42, 385-389.

Böhlke, T., Bondár, G., Estrin, Y., Lebyodkin, M.A., 2009. Geometrically non-linear modeling of the Portevin–Le Chatelier effect. *Comput. Mater. Sci.* 44, 1076-1088.

Bron, F., Besson, J., 2004. A yield function for anisotropic materials Application to aluminum alloys. *International Journal of Plasticity* 20, 937-963.

Cai, Y., Yang, S., Fu, S., Zhang, D., Zhang, Q., 2017. Investigation of Portevin–Le Chatelier Band Strain and Elastic Shrinkage in Al-Based Alloys Associated with Mg Contents. *Journal of Materials Science & Technology* 33, 580-586.

Cazacu, O., 2018. New yield criteria for isotropic and textured metallic materials. *International Journal of Solids and Structures* 139-140, 200-210.

Cazacu, O., Plunkett, B., Barlat, F., 2006. Orthotropic yield criterion for hexagonal closed packed metals. *Int. J. Plasticity* 22, 1171-1194.

Chaboche, J.L., 2008. A review of some plasticity and viscoplasticity constitutive theories. *Int. J. Plasticity* 24, 1642-1693.

Cheng, J., Nemat-Nasser, S., 2000. A model for experimentally-observed high-strain-rate dynamic strain aging in titanium. *Acta Materialia* 48, 3131-3144.

Cheng, J., Nemat-Nasser, S., Guo, W., 2001. A unified constitutive model for strain-rate and temperature dependent behavior of molybdenum. *Mechanics of Materials* 33, 603-616.

Cui, C.Y., Gu, Y.F., Yuan, Y., Harada, H., 2011. Dynamic strain aging in a new Ni–Co base superalloy. *Scripta Materialia* 64, 502-505.

Gao, X., Zhang, T., Zhou, J., Graham, S.M., Hayden, M., Roe, C., 2011. On stress-state dependent plasticity modeling: Significance of the hydrostatic stress, the third invariant of stress deviator and the non-associated flow rule. *Int. J. Plasticity* 27, 217-231.

Gilat, A., Wu, X., 1997. Plastic deformation of 1020 steel over a wide range of strain rates and temperatures. *International Journal of Plasticity* 13, 611-632.

Guo, W.-G., Gao, X., 2013. On the constitutive modeling of a structural steel over a range of strain rates and temperatures. *Materials Science and Engineering: A* 561, 468-476.

Guo, W.-G., Nemat-Nasser, S., 2006. Flow stress of Nitronic-50 stainless steel over a wide range of strain rates and temperatures. *Mechanics of Materials* 38, 1090-1103.

Ha, J., Baral, M., Korkolis, Y.P., 2018. Plastic anisotropy and ductile fracture of bake-hardened AA6013 aluminum sheet. *Int. J. Solids Struct.* 155, 123-139.

Habib, S.A., Khan, A.S., Gnäupel-Herold, T., Lloyd, J.T., Schoenfeld, S.E., 2017. Anisotropy, tension-compression asymmetry and texture evolution of a rare-earth-containing magnesium alloy sheet, ZEK100, at different strain rates and temperatures: Experiments and modeling. *International Journal of Plasticity* 95, 163-190.

Hill, R., 1948. A Theory of the Yielding and Plastic Flow of Anisotropic Metals. *Proceedings of the Royal Society of London Series A-Mathematical and Physical Sciences* 193, 281-297.

Hong, S.I., 1985. Influence of Dynamic Strain Aging on the Apparent Activation Volume for Deformation. *Materials Science and Engineering* 76, 77-81.

Hora, P., Tong, L., Berisha, B., 2011. Modified maximum force criterion, a model for the theoretical prediction of forming limit curves. *International Journal of Material Forming* 6, 267-279.

Jeong, Y., Pham, M.-S., Iadicola, M., Creuziger, A., Foecke, T., 2016. Forming limit prediction using a self-consistent crystal plasticity framework: a case study for body-centered cubic materials. *Modell. Simul. Mater. Sci. Eng.* 24, 055005.

Johnson, G.R., Cook, W.H., 1985. Fracture characteristics of three metals subjected to various strains, strain rates, temperatures and pressures. *Engineering Fracture Mechanics* 21, 31-48.

Karafillis, A.P., Boyce, M.C., 1993. A General Anisotropic Yield Criterion Using Bounds and a Transformation Weighting Tensor. *J. Mech. Phys. Solids* 41, 1859-1886.

Khan, A.S., Baig, M., 2011. Anisotropic responses, constitutive modeling and the effects of strain-rate and temperature on the formability of an aluminum alloy. *International Journal of Plasticity* 27, 522-538.

Khan, A.S., Huang, S., 1992. Experimental and theoretical study of mechanical behavior of 1100 aluminum in the strain rate range  $10^{-5}$ – $10^4$ s $^{-1}$ . *Int. J. Plasticity* 8, 397-424.

Khan, A.S., Kazmi, R., Farrokh, B., 2007. Multiaxial and non-proportional loading responses, anisotropy and modeling of Ti–6Al–4V titanium alloy over wide ranges of strain rates and temperatures. *International Journal of Plasticity* 23, 931-950.

Khan, A.S., Liang, R., 1999. Behaviors of three BCC metal over a wide range of strain rates and temperatures: experiments and modeling. *Int. J. Plasticity* 15, 1089-1109.

- Khan, A.S., Liu, H., 2012. Variable strain rate sensitivity in an aluminum alloy: response and constitutive modeling. *International Journal of Plasticity* 36, 1-14.
- Khan, A.S., Yu, S., 2012. Deformation induced anisotropic responses of Ti–6Al–4V alloy. Part I: Experiments. *International Journal of Plasticity* 38, 1-13.
- Khan, A.S., Yu, S., Liu, H., 2012. Deformation induced anisotropic responses of Ti–6Al–4V alloy Part II: A strain rate and temperature dependent anisotropic yield criterion. *International Journal of Plasticity* 38, 14-26.
- Kobelev, N.P., Lebyodkin, M.A., Lebedkina, T.A., 2017. Role of Self-Organization of Dislocations in the Onset and Kinetics of Macroscopic Plastic Instability. *Metallurgical and Materials Transactions A* 48, 965-974.
- Kondori, B., Madi, Y., Besson, J., Benzerga, A.A., 2019. Evolution of the 3D plastic anisotropy of HCP metals: Experiments and modeling. *International Journal of Plasticity* 117, 71-92.
- Kreyca, J., Kozeschnik, E., 2018. State parameter-based constitutive modelling of stress strain curves in Al-Mg solid solutions. *International Journal of Plasticity* 103, 67-80.
- Kubin, L.P., Estrin, Y., 1990. Evolution of dislocation densities and the critical conditions for the Portevin-Le Châtelier effect. *Acta Metallurgica et Materialia* 38, 697-708.
- Kubin, L.P., Estrin, Y., 1992. The Critical Conditions for Jerky Flow. Discussion and Application to CuMn Solid Solutions. *physica status solidi (b)* 172, 173-185.
- Lee, E.-H., Stoughton, T.B., Yoon, J.W., 2017. A yield criterion through coupling of quadratic and non-quadratic functions for anisotropic hardening with non-associated flow rule. *International Journal of Plasticity* 99, 120-143.
- Lee, K.-O., Lee, S.-B., 2012. Modeling of materials behavior at various temperatures of hot isostatically pressed superalloys. *Materials Science and Engineering: A* 541, 81-87.
- Lee, S.-J., Kim, J., Kane, S.N., Cooman, B.C.D., 2011. On the origin of dynamic strain aging in twinning-induced plasticity steels. *Acta Materialia* 59, 6809-6819.
- Li, H., Zhang, H.Q., Yang, H., Fu, M.W., Yang, H., 2017. Anisotropic and asymmetrical yielding and its evolution in plastic deformation: Titanium tubular materials. *International Journal of Plasticity* 90, 177-211.
- Li, X., Roth, C.C., Mohr, D., 2019. Machine-learning based temperature- and rate-dependent plasticity model: Application to analysis of fracture experiments on DP steel. *International Journal of Plasticity* 118, 320-344.
- Lian, J., Shen, F., Münstermann, S., 2018a. Evolution of plastic anisotropy and strain rate

sensitivity. *J. Phys. Conf. Ser.* 1063.

Lian, J.H., Shen, F.H., Jia, X.X., Ahn, D.C., Chae, D.C., Munstermann, S., Bleck, W., 2018b. An evolving non-associated Hill48 plasticity model accounting for anisotropic hardening and r-value evolution and its application to forming limit prediction. *International Journal of Solids and Structures* 151, 20-44.

Liang, R.Q., Khan, A.S., 1999. A critical review of experimental results and constitutive models for BCC and FCC metals over a wide range of strain rates and temperatures. *International Journal of Plasticity* 15, 963-980.

Liu, W., Lian, J., Muenstermann, S., Zeng, C., Fang, X., 2020. Prediction of crack formation in the progressive folding of square tubes during dynamic axial crushing *Int. J. Mech. Sci.* accepted.

Lou, Y., Yoon, J.W., 2018. Anisotropic yield function based on stress invariants for BCC and FCC metals and its extension to ductile fracture criterion. *Int. J. Plasticity* 101, 125-155.

Marciniak, Z., Kuczynski, K., 1967. Limit strains in the processes of stretch-forming sheet metal. *International Journal of Mechanical Sciences* 9, 609-612.

Mazière, M., Dierke, H., 2012. Investigations on the Portevin Le Chatelier critical strain in an aluminum alloy. *Comput. Mater. Sci.* 52, 68-72.

McCormick, P.G., 1988. Theory of flow localisation due to dynamic strain ageing. *Acta Metallurgica* 36, 3061-3067.

Meng, W., Guo, G., 2011. Study of plastic flow unified constitutive relation for steel DH-36. *Chinese Journal of Theoretical and Applied Mechanics* 43, 1-5.

Mogucheva, A., Yuzbekova, D., Kaibyshev, R., Lebedkina, T., Lebyodkin, M., 2016. Effect of Grain Refinement on Jerky Flow in an Al-Mg-Sc Alloy. *Metallurgical and Materials Transactions A* 47, 2093-2106.

Muenstermann, S., Schuff, C., Lian, J., Doebereiner, B., Brinnel, V., Wu, B., 2013. Predicting lower bound damage curves for high-strength low-alloy steels. *Fatigue & Fracture of Engineering Materials & Structures* 36, 779-794.

Nemat-Nasser, S., Guo, W.-G., 2003. Thermomechanical response of DH-36 structural steel over a wide range of strain rates and temperatures. *Mechanics of Materials* 35, 1023-1047.

Nemat-Nasser, S., Guo, W.-G., 2005. Thermomechanical response of HSLA-65 steel plates: experiments and modeling. *Mechanics of Materials* 37, 379-405.

Nemat-Nasser, S., Guo, W.G., Cheng, J.Y., 1999. Mechanical properties and deformation mechanisms of a commercially pure titanium. *Acta Materialia* 47, 3705-3720.

- Nemat-Nasser, S., Guo, W.G., Kihl, D.P., 2001. Thermomechanical response of AL-6XN stainless steel over a wide range of strain rates and temperatures. *J Mech Phys Solids* 49, 1823-1846.
- Novoksharov, D., Döbereiner, B., Sharaf, M., Münstermann, S., Lian, J., 2015. A new model for upper shelf impact toughness assessment with a computationally efficient parameter identification algorithm. *Engineering Fracture Mechanics* 148, 281-303.
- Otto, F., Dlouhý, A., Somsen, C., Bei, H., Eggeler, G., George, E.P., 2013. The influences of temperature and microstructure on the tensile properties of a CoCrFeMnNi high-entropy alloy. *Acta Materialia* 61, 5743-5755.
- Park, N., Stoughton, T.B., Yoon, J.W., 2019a. A Criterion for General Description of Anisotropic Hardening Considering Strength Differential Effect with Non-associated Flow Rule. *International Journal of Plasticity*.
- Park, T., Abu-Farha, F., Pourboghrat, F., 2019b. An Evolutionary Yield Function Model Based on Plastic Work and Non-Associated Flow Rule. *Metals* 9.
- Picu, R.C., 2004. A mechanism for the negative strain-rate sensitivity of dilute solid solutions. *Acta Materialia* 52, 3447-3458.
- Picu, R.C., Zhang, D., 2004. Atomistic study of pipe diffusion in Al-Mg alloys. *Acta Materialia* 52, 161-171.
- Plunkett, B., Lebensohn, R.A., Cazacu, O., Barlat, F., 2006. Anisotropic yield function of hexagonal materials taking into account texture development and anisotropic hardening. *Acta Materialia* 54, 4159-4169.
- Reed, R.P., 1972. Aluminium 2. A review of deformation properties of high purity aluminium and dilute aluminium alloys. *Cryogenics* 12, 259-291.
- Safaei, M., Yoon, J.W., De Waele, W., 2014. Study on the definition of equivalent plastic strain under non-associated flow rule for finite element formulation. *International Journal of Plasticity* 58, 219-238.
- Safaei, M., Zang, S.-l., Lee, M.-G., De Waele, W., 2013. Evaluation of anisotropic constitutive models: Mixed anisotropic hardening and non-associated flow rule approach. *International Journal of Mechanical Sciences* 73, 53-68.
- Saleh, A.A., Pereloma, E.V., Gazder, A.A., 2013. Microstructure and texture evolution in a twinning-induced-plasticity steel during uniaxial tension. *Acta Materialia* 61, 2671-2691.
- Shen, F., Lian, J., Münstermann, S., Kokotin, V., Pretorius, T., 2018. An Experimental and

Numerical Investigation of the Anisotropic Plasticity and Fracture Properties of High Strength Steels from Laboratory to Component Scales. *Procedia Structural Integrity* 13, 1312-1317.

Shen, F., Lian, J., Münstermann, S., Kokotin, V., Pretorius, T., 2019a. Anisotropic plasticity model considering the dynamic strain ageing effects. *AIP Conference Proceedings* 2113, 160017.

Shen, F., Münstermann, S., Lian, J., 2019b. Forming limit prediction by the Marciniak–Kuczynski model coupled with the evolving non-associated Hill48 plasticity model. *Journal of Materials Processing Technology*, 116384.

Stoughton, T.B., 2002. A non-associated flow rule for sheet metal forming. *International Journal of Plasticity* 18, 687-714.

Stoughton, T.B., Yoon, J.W., 2009. Anisotropic hardening and non-associated flow in proportional loading of sheet metals. *Int. J. Plasticity* 25, 1777-1817.

Sung, J.H., Kim, J.H., Wagoner, R.H., 2010. A plastic constitutive equation incorporating strain, strain-rate, and temperature. *International Journal of Plasticity* 26, 1746-1771.

Suzuki, T., Okamura, K., Capilla, G., Hamasaki, H., Yoshida, F., 2018. Effect of anisotropy evolution on circular and oval hole expansion behavior of high-strength steel sheets. *International Journal of Mechanical Sciences* 146-147, 556-570.

Tsai, C.-W., Lee, C., Lin, P.-T., Xie, X., Chen, S., Carroll, R., LeBlanc, M., Brinkman, B.A.W., Liaw, P.K., Dahmen, K.A., Yeh, J.-W., 2019. Portevin-Le Chatelier mechanism in face-centered-cubic metallic alloys from low to high entropy. *International Journal of Plasticity*.

Wang, J., Guo, W.-G., Gao, X., Su, J., 2015. The third-type of strain aging and the constitutive modeling of a Q235B steel over a wide range of temperatures and strain rates. *Int. J. Plasticity* 65, 85-107.

Wang, X.G., Wang, L., Huang, M.X., 2017. Kinematic and thermal characteristics of Lüders and Portevin-Le Chatelier bands in a medium Mn transformation-induced plasticity steel. *Acta Materialia* 124, 17-29.

Wesselmecking, S., Song, W.W., Ma, Y., Roesler, T., Hofmann, H., Bleck, W., 2018. Strain Aging Behavior of an Austenitic High-Mn Steel. *Steel Research International* 89, 1700515.

Xie, Q., Van Bael, A., An, Y.G., Lian, J., Sidor, J.J., 2018. Effects of the isotropic and anisotropic hardening within each grain on the evolution of the flow stress, the r-value and the deformation texture of tensile tests for AA6016 sheets. *Materials Science and Engineering: A* 721, 154-164.

Yang, F., Luo, H., Pu, E., Zhang, S., Dong, H., 2018. On the characteristics of Portevin–Le Chatelier bands in cold-rolled 7Mn steel showing transformation-induced plasticity. *Int. J.*

Plasticity 103, 188-202.

Yoon, J.W., Lou, Y., Yoon, J., Glazoff, M.V., 2014. Asymmetric yield function based on the stress invariants for pressure sensitive metals. *International Journal of Plasticity* 56, 184-202.

Yoshida, F., Uemori, T., 2002. A model of large-strain cyclic plasticity describing the Bauschinger effect and workhardening stagnation. *International Journal of Plasticity* 18, 661-686.

Yuzbekova, D., Mogucheva, A., Zhemchuzhnikova, D., Lebedkina, T., Lebyodkin, M., Kaibyshev, R., 2017. Effect of microstructure on continuous propagation of the Portevin–Le Chatelier deformation bands. *Int. J. Plasticity* 96, 210-226.

Zerilli, F.J., Armstrong, R.W., 1987. Dislocation-mechanics-based constitutive relations for material dynamics calculations. *Journal of Applied Physics* 61, 1816-1825.

Zhang, S., Lou, Y., Yoon, J.W., 2017. Finite Element formulation of a general asymmetrical yield function for pressure sensitive metals. *Procedia Engineering* 207, 215-220.

Zhemchuzhnikova, D., Lebyodkin, M., Lebedkina, T., Mogucheva, A., Yuzbekova, D., Kaibyshev, R., 2017. Peculiar Spatiotemporal Behavior of Unstable Plastic Flow in an AlMgMnScZr Alloy with Coarse and Ultrafine Grains. *Metals* 7, 325.

Zhemchuzhnikova, D., Lebyodkin, M., Yuzbekova, D., Lebedkina, T., Mogucheva, A., Kaibyshev, R., 2018. Interrelation between the Portevin Le-Chatelier effect and necking in AlMg alloys. *Int. J. Plasticity* 110, 95-109.